

Article

Geochronology and Petrogenesis of Ahetala Granodiorite in South Tianshan Orogenic Belt, Xinjiang: New Constraints on the Tectonic Evolution of the South Tianshan Ocean

Yang Xu ^{1,2}, Jingwu Yin ^{2,*}, Keyan Xiao ^{1,*}, Chunlian Wang ¹ , Haiming Xu ¹, Jingling Fang ¹ and Mingjing Fan ^{1,3}¹ Institute of Mineral Resources, Chinese Academy of Geological Sciences, Beijing 100037, China² Institute of Earth Science, China University of Geosciences, Beijing 100083, China³ Institute of Geological Survey, China University of Geosciences, Wuhan 430074, China

* Correspondence: yinjwt@cugb.edu.cn (J.Y.); xiaokeyan@mail.cgs.gov.cn (K.X.)

Abstract: The Ahetala granodiorite is located in the western section of the South Tianshan Orogenic Belt (STOB), which is of great significance regarding the dispute on the closing date of the South Tianshan Ocean (STO) and the tectonic evolution of STOB. To determine the tectonic setting and petrogenesis, the study of petrography, electron probe microanalysis (EPMA), LA-ICP-MS zircon U–Pb geochronology, and major and trace elements analyses are carried out for Ahetala granodiorite. Based on LA-ICP-MS U–Pb zircon dating, the granodiorite was emplaced at 282.1 ± 1.3 Ma (MSWD = 1.11). Geochemically, Ahetala granodiorite is characterized by metaluminous ($A/CNK = 0.86–0.87$), rich alkali ($K_2O + Na_2O = 6.80–7.13$), which belongs to high-K calc-alkaline I-type granite. They are enriched in LREE and depleted in HREE ($LREE/HREE = 9.02–13.89$) and exhibit insignificant Eu anomalies ($\delta Eu = 0.94–0.97$). Ahetala granodiorite is enriched in large ion lithophile elements (e.g., K, Sr, Ba) and depleted in high field-strength elements (e.g., Ta, Ti, Nb, P). The Nb/Ta values (10.97–18.10), Zr/Hf values (39.41–40.19), and Mg# (54.87–56.02) of the granodiorite and the MgO content of biotites (13.42–14.16), the M value ($M = Mg/(Mg + Fe^{2+})$) of amphiboles (0.68–0.75), suggest that granodiorite originates from the crustal contamination of the mantle-derived magmas. Combined with regional geological background, previous research, and the nature of the Ahetala granodiorite, we suggest that Ahetala granodiorite was emplaced at a transitional stage of the volcanic arc (syn-collision) to post-collision setting and the South Tianshan Ocean was closed in the Early Permian.



Citation: Xu, Y.; Yin, J.; Xiao, K.; Wang, C.; Xu, H.; Fang, J.; Fan, M. Geochronology and Petrogenesis of Ahetala Granodiorite in South Tianshan Orogenic Belt, Xinjiang: New Constraints on the Tectonic Evolution of the South Tianshan Ocean. *Minerals* **2022**, *12*, 1588. <https://doi.org/10.3390/min12121588>

Academic Editors:

Antonios Koroneos, Ioannis Baziotis and Kristina Šarić

Received: 30 October 2022

Accepted: 5 December 2022

Published: 11 December 2022

Publisher's Note: MDPI stays neutral with regard to jurisdictional claims in published maps and institutional affiliations.



Copyright: © 2022 by the authors. Licensee MDPI, Basel, Switzerland. This article is an open access article distributed under the terms and conditions of the Creative Commons Attribution (CC BY) license (<https://creativecommons.org/licenses/by/4.0/>).

Keywords: granodiorite; zircon U–Pb geochronology; geochemistry; electron probe microanalysis (EPMA); Permian; South Tianshan Orogenic Belt; tectonic evolution

1. Introduction

The Central Asian Orogenic Belt (CAOB) is one of the essential metallogenic belts in the world and was developed by the closure of the Paleo-Asian Ocean [1–5]. Based on the evidence of ophiolite mélanges, high-ultrahigh pressure metamorphic belts, etc., different studies indicated that the Ancient Tianshan Ocean (Terskey Ocean), the North Tianshan Ocean (Junggar Ocean), and the South Tianshan Ocean (STO) together constitute the southwestern part of the Paleo-Asian Ocean [1,6,7]. The formation, evolution, and extinction of the Paleo-Asian Ocean were accompanied by the multiple accretionary and collisional events of many landmasses (Siberia, Tarim, etc.). The South Tianshan Orogenic Belt (STOB) was formed after the northward subduction of the Tarim Craton underneath the Yili-Central Tianshan plate and the closure of the STO [8–14]. The formation of the STOB may mark the termination of the central Asian accretionary orogenesis because the Tarim Craton is regarded as the last plate on CAOB following the final closure of the STO [15,16]. Therefore, it is critical to recognize the history of STO.

In order to identify the petrogenesis and tectonic setting, past studies used different methods and techniques to analyze ophiolite mélanges, high-ultrahigh pressure metamorphic minerals, fossils, detrital zircons, granites, etc., in STOB. It is widely accepted that the ophiolite is the direct product of the subduction and collision of oceanic and continental plates, so ophiolite has been used to analyze the subduction of the oceanic lithosphere and the formation and evolution of the arc basin system at the continental margin. According to Qiqijianake [17], Baleigong [18], Kulehu [19], Jigen [20], and Misibulake, Serikeyayibulake, Aertengkesibulake, Changawuzibulake [21], etc., ophiolite mélanges have been discovered in the STOB (Figure 1). It can be seen that these ophiolite mélanges are aged between 390 and 450 Ma, which implies that the Paleozoic ocean basin still existed in the STO during the Silurian to Devonian. Eclogites from the ultra-high pressure metamorphic belt in the southwest Tianshan confirm that the oceanic crust subducted at the Permian (280–290 Ma) [22]. Radiolarian fossils in the Wupatarkan and Aiketike group indicate that the ancient ocean basin may have existed in the STO during the Permian period [23,24].

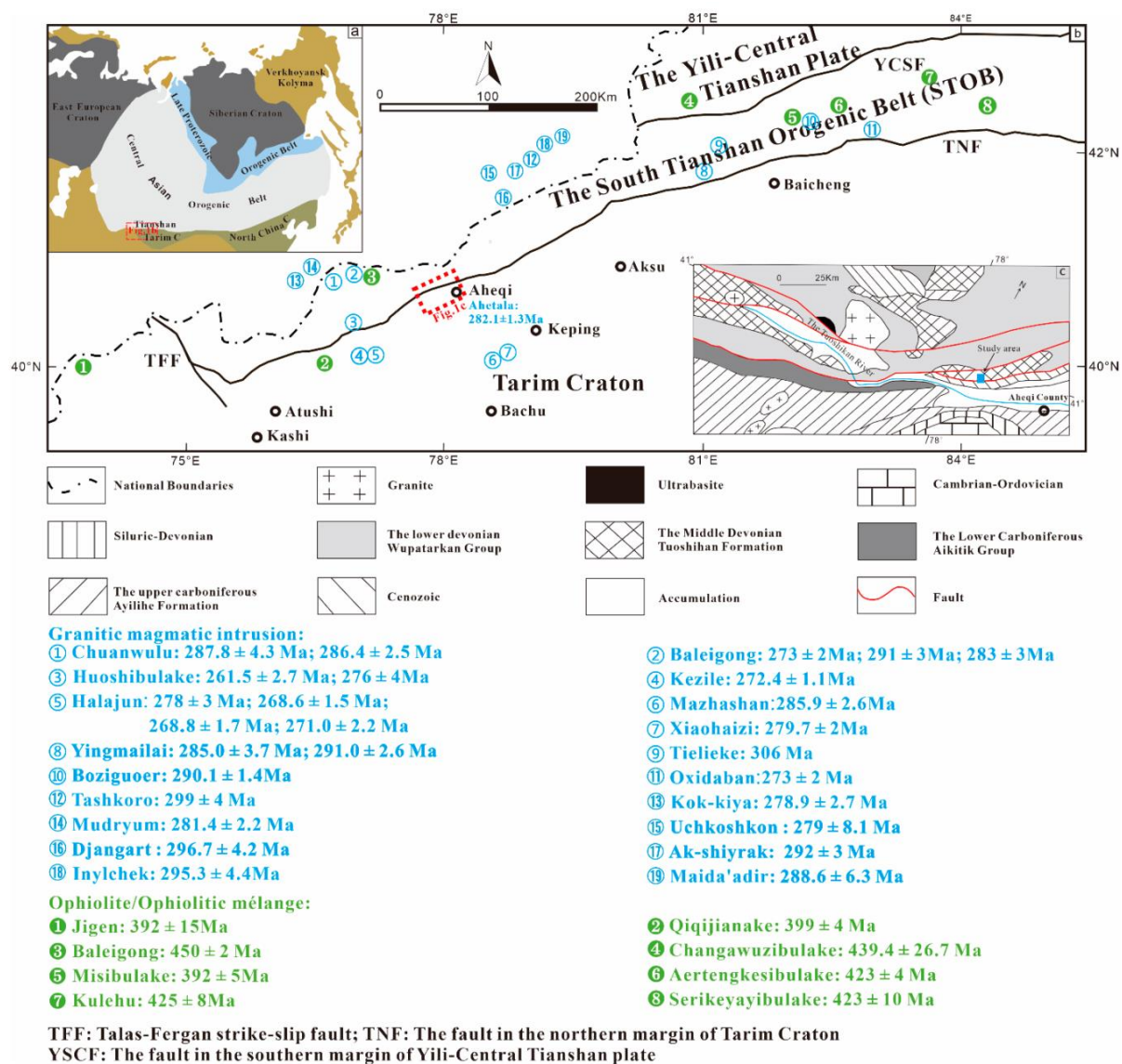


Figure 1. (a) Sketch map of orogenic collages in Asia (modified from [5]); (b) distribution map of granitoid rocks and ophiolite in the STOB (modified from [25]); (c) regional geological sketch map of the Aheqi county (modified from [23]). Data sources: ①: [25]; ②: [26,27]; ③: [28,29]; ④–⑤: [29,42]; ⑥: [43]; ⑦: [44]; ⑧: [38,45]; ⑨: [45]; ⑩: [46]; ⑪: [47]; ⑫–⑱: [48–51]; ①: [20]; ②: [17]; ③: [18]; ⑦: [19], ④–⑧: [21].

In addition, different studies have mainly focused on the granitic magmatic activity in STOB. The Chuanwulu igneous complex (286.4 ± 2.5 Ma [25]), Baleigong granite (273 ± 2 Ma [26], 291 ± 3 Ma, 283 ± 3 Ma [27]), and Huoshibulake granite (261.5 ± 2.7 Ma [28], 276 ± 4 Ma [29]), etc., have been discovered in the STOB (Figure 1). The formation of granite was closely related to the tectonic environment and geodynamic process. It is believed that Late Paleozoic collisional granites in this area were formed by the collision between the Tarim Craton and Yili-Central Tianshan plate. However, most of these granites are A-type granites. There are few reports concerning the research of I-type granites in the STOB, which restricts a comprehensive understanding of the tectonic evolution in the STO. The most fundamental question regarding the closure time of the STO is still under debate. Past studies constrain the three possible closure time of STO: prior to the Permian [25,30–35], during the Permian [10,23,24,26,36–38], and during the Triassic [15,22,39–41].

The I-type granodiorite intrusion was discovered at the Ahetala copper deposit in the STOB, which was related to the subduction of the Tarim plate and closure of the STO. To add some insightful information to the above disputes and comprehensively discuss the tectonic evolution and closing time of STO, we systematically sampled and analyzed zircon U–Pb ages, the chemical composition of rock-forming minerals, and the major, trace elements of the Ahetala granodiorite.

2. Geological Setting

The CAOBS (i.e., the Altaid Collage [5]) is the largest Phanerozoic accretionary orogen in the world. It is sandwiched between the Eastern European, Siberian, Tarim, and North China Cratons (Figure 1a). Traditionally, the CAOBS is subdivided into eastern and western parts by taking 88° E as the boundary. The western CAOBS comprises the Altai Mountain, Junggar Basin, Tianshan Mountains, and Tarim Basin [25,52]. The Tianshan Mountains are located in the southern margin of the western CAOBS (Figure 1a), extending for ca. 2500 km from the Aral Sea in Uzbekistan to north Xinjiang in China [35,48]. Tectonically, the Tianshan Mountains can be divided into four geological units from south to north: (1) northern margin of Tarim Craton, (2) STOB, (3) Central Tianshan Block (CTB), and (4) North Tianshan Orogenic Belt (NTOB). The STOB is bounded by the Yili-Central Tianshan Suture Belt in the north and the North Tarim Fault in the south (Figure 1b) [25].

The STOB is regarded as a collisional belt and separates the Central Tianshan plate and the Tarim Craton [1,8,9,25,53], which is related to the closure of the STO. Many high-ultrahigh pressure metamorphic rocks (blueschist-, eclogite-, and greenschist-facies meta-sedimentary rocks) have been found in Paleozoic ophiolites/ophiolitic mélanges along the STOB, which has a connection with the closure of the STO [10,27]. The emplacement date of the basic-ultrabasic igneous rocks in ophiolite mainly from the Silurian to the Devonian periods.

The base of the STOB in China is the metamorphic rocks of the Paleo-Proterozoic Xingditagh Formation, which is covered by the Middle Proterozoic Akesu Formation [54]. The South Tianshan mainly includes the Cambrian to Carboniferous and Cenozoic strata [55]. Early Paleozoic limestone, clastic sedimentary rocks, and volcanic rocks are widespread in the STOB. The Cambrian, Ordovician, and Silurian strata are mainly carbonate and clastic rocks. The Devonian strata are mainly clastic sedimentary rocks, volcanic rock, and carbonatite. The Carboniferous strata are mainly sandstone, shale, slate, and limestone.

Most of the outcrop of igneous rocks are granitoids that cover almost 5% of the total STOB [25]. The emplacement age of most intrusive rocks ranges from the Late Carboniferous to Early Permian. The STOB was uplifted by collision and orogeny. In this period, the orogenic magmatic activity gradually decreased and the post-orogenic or non-orogenic magmatic activity increased. From the Heiyang mountain to Aheqi county, the intrusive rocks often come into contact with surrounding rocks, thus forming skarn.

3. Local Geology and Petrography

The study area is located about 50 km to the northwest of Aheqi County, Kirgiz Autonomous Prefecture, Xinjiang Uygur Autonomous Region of China. The Aheta granodiorite is located in the south of the Kokshal anticlinorium and at the juncture of the Toshihan fault and the Tatiertashiqaoke inverse fault. The granodiorite is related to the mineralization of the skarn copper deposit. The strata in the study area mainly include: (1) the bioclastic limestone and marble of the Tuoshihan Formation. The marble and granodiorite contact in the center of the study area, which is closely related to the mineralization of the copper deposit; (2) the conglomerate, muddy siltstone, and silty mudstone of the Wuqia formation [56,57].

The study area consists of a monoclinical structure with SE dip angle of 15–30°. Several NNW faults are developed and have a relatively significant influence on the area. The Aheta granodiorite is exposed as stock intrudes into the marble of the Toshihan Formation. The east of the granodiorite is covered by the conglomerate of the Wuqia Formation [56,57] (Figures 1c and 2).

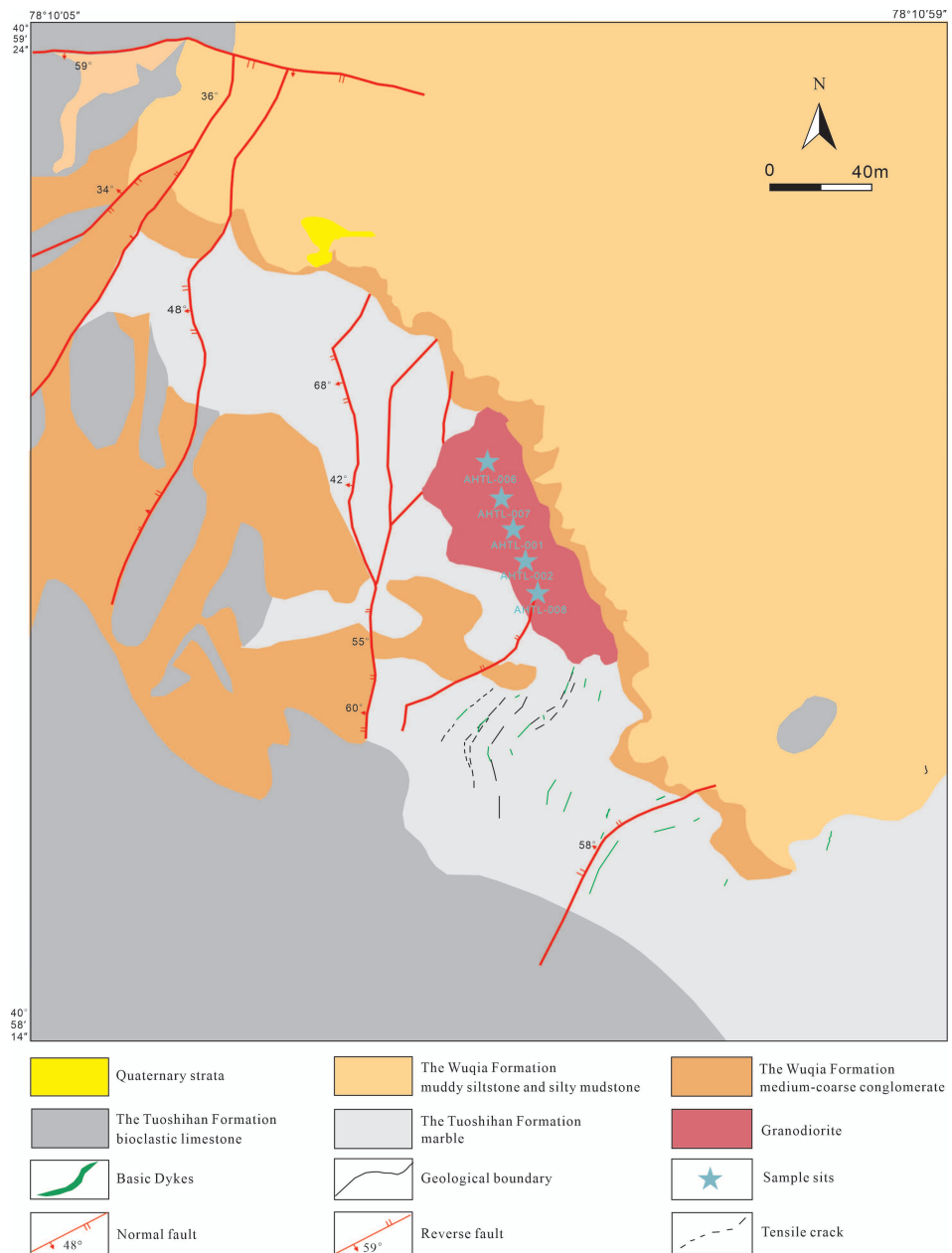


Figure 2. Geological map of Aheta granodiorite with its main lithologic units (modified from [56,57]).

The outcrops define an oval shape with an area of $\sim 0.21 \text{ km}^2$. The skarn is observed at the contact belt between the intrusion and surrounding rock. All specimens were sampled at different locations along the strike of Ahetala granodiorite. According to field (Figure 3a) and microscopic observations, the intrusion is granodiorite. Unweathered samples (Figure 3b) in this study show a medium-fine-grained texture and massive structure and are mainly composed of plagioclase ($\sim 45\text{--}50 \text{ vol.}\%$), potassium feldspar ($\sim 15\text{--}20 \text{ vol.}\%$), quartz ($\sim 20\text{--}25 \text{ vol.}\%$), hornblende ($\sim 5 \text{ vol.}\%$), and biotite ($\sim 5 \text{ vol.}\%$) with accessory magnetite, zircon, apatite, and titanite (Figure 3c–f). Plagioclase grains are white, euhedral, or hypidiomorphic, with a large diameter, and generally display oscillatory zoning (Figure 3c–f). Potassium feldspars are colorless and have a typical polysynthetic twin (Figure 3c,d). Biotite is brown, plate-like, and shows a clear cleavage $\{001\}$ (Figure 3e,f). Hornblende is light brown and fusiform (Figure 3d,f).

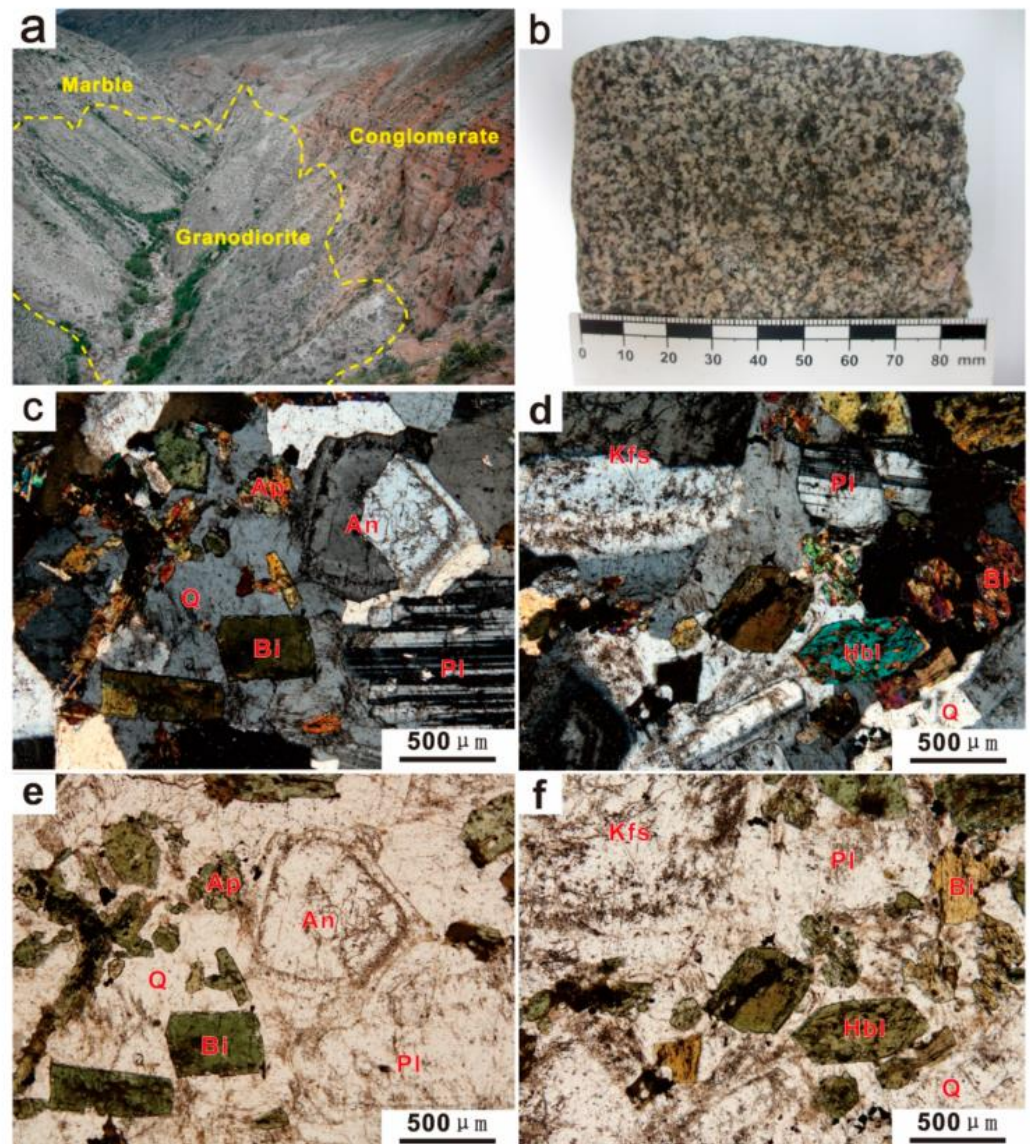


Figure 3. Field photographs and the microscopic images of granodiorite samples. (a,b) Photographs of intrusive rock and sample of Ahetala granodiorite; (c,d) photomicrograph (cross-polarized light) of typical granodiorite texture; (e,f) photomicrograph (plane-polarized light) of typical granodiorite texture. Abbreviations are as follows: Q—Quartz; Bi—Biotite; Pl—Plagioclase; An—Anorthite; Kfs—Potassium feldspar; Hbl—Hornblende; Ap—Apatite.

4. Analytical Techniques

4.1. Zircon U–Pb Dating

Zircons were separated from five samples of granodiorite for Laser Ablation-Inductively Coupled Plasma-Mass Spectrometer (LA-ICP-MS) U–Pb age dating. The zircon grains were separated through conventional density and magnetic separation techniques and carefully picked under the binocular microscope. High quality zircons were selected, mounted in epoxy resins, and finally, polished for analysis. All zircons were studied under transmitted and cathodoluminescence (CL) imaging to observe the morphology and internal structures and to select spots for U–Pb dating. The above work was completed at Beijing GeoAnalysis Co., LTD. (Beijing, China).

The zircon U–Pb dating was tested with an X Series 2 ICP-MS, analyzed with 32 μm laser spot diameter at a frequency of 6 Hz, and housed at the LA-ICP-MS Laboratory of the Institute of Earth Sciences of the China University of Geosciences (Beijing, China). Zircon 91 500 was used as the reference sample for U–Pb dating and optimizing the instrument. A standard zircon mud tank was used for the monitoring sample. The experimental data were processed by ICPMSDataCal software [58].

4.2. Mineral Geochemistry

Fresh samples of granodiorite were selected for making thin sections without coverslip. The surface of the thin section was coated with carbon for better conductivity in the experiment. The chemical composition of rock-forming minerals in granodiorite was analyzed with EPMA-1600 at the China University of Geosciences (Beijing, China). During the electron probe microanalysis, the acceleration voltage was 15 kV and the beam current was 1×10^{-8} A. All the standard samples conformed to the SPI standard of the USA in the experiment.

4.3. Whole-Rock Analyses

Five fresh samples of granodiorite were selected for whole-rock analysis. Major elements were analyzed by Leeman Prodigy ICP-OES, and trace and rare-earth elements were analyzed by Agilent Technologies ICP-MS-7500a at the Experimental Testing Centre of the Institute of Earth Sciences of the China University of Geosciences (Beijing, China). The final results were processed using Agilent 7500a software.

5. Results

5.1. Zircon U–Pb Geochronology

The results of zircon U–Pb dating from the Ahetala granodiorite are shown in Table 1. In CL images (Figure 4a), twenty zircons are colorless, euhedral, and prismatic with clear oscillatory zoning and no inclusions. The lengths of zircon are mostly in the range 100–150 μm , and their length/width ratios are close to 2:1. AHTL-19 displays discordant older $^{206}\text{Pb}/^{238}\text{U}$ age, and it is likely to be a xenocrystal. In addition, AHTL-2, -4, -7, and -13 are all below the concordia line of U–Pb zircon, which is caused by lead loss. The concordance of AHTL-2, -4, -7, -13, and -19 are less than 95%. In order to improve the reliability and accuracy of the experimental results, AHTL-2, -4, -7, -13, and -19 were not involved in zircon U–Pb dating (Figure 4b). The zircon samples show 280.3 to 857.76 ppm (average of 500.94 ppm) for Th and 489.91 to 1270.99 ppm (average of 746.59 ppm) for U. Fifteen zircons have high Th/U ratios (0.58–0.75) and typical oscillatory zoning, implying magmatic origin. All spot analyses show concordant ages from 273 to 290 Ma with a weighted mean $^{206}\text{Pb}/^{238}\text{U}$ age of 282.1 ± 1.3 Ma (MSWD = 1.11), which is considered to represent the emplacement age of the granodiorite (Figure 4c).

Table 1. LA-ICP-MS analytical data for zircons from samples of the Ahetala granodiorite.

Sample	w(Th)/10 ⁻⁶	w(U)/10 ⁻⁶	Th/U	²⁰⁷ Pb/ ²³⁵ U		²⁰⁶ Pb/ ²³⁸ U		²⁰⁶ Pb/ ²³⁸ U	
				Ratio	1σ	Ratio	1σ	Age/Ma	Ma
AHTL-1	595.94	831.93	0.72	0.3259	0.0201	0.0458	0.0008	288.5	4.9
* AHTL-2	814.47	1018.88	0.80	0.3254	0.0190	0.0417	0.0008	263.4	4.8
AHTL-3	522.77	703.06	0.74	0.3177	0.0185	0.0437	0.0007	275.5	4.3
* AHTL-4	637.86	903.94	0.71	0.3399	0.0221	0.0434	0.0008	274.0	4.9
AHTL-5	670.53	898.12	0.75	0.3224	0.0211	0.0447	0.0009	281.7	5.5
AHTL-6	402.10	590.27	0.68	0.3306	0.0232	0.0439	0.0011	277.0	6.6
* AHTL-7	476.90	721.77	0.66	0.3396	0.0206	0.0421	0.0009	265.6	5.6
AHTL-8	597.23	860.11	0.69	0.3267	0.0169	0.0455	0.0007	286.6	4.1
AHTL-9	420.98	653.86	0.64	0.3183	0.0222	0.0444	0.0007	280.1	4.2
AHTL-10	382.11	639.10	0.60	0.3248	0.0207	0.0449	0.0008	282.8	5.0
AHTL-11	702.22	982.57	0.71	0.3240	0.0189	0.0452	0.0009	284.7	5.3
AHTL-12	280.30	481.91	0.58	0.3226	0.0195	0.0460	0.0009	289.6	5.6
* AHTL-13	525.82	754.34	0.70	0.3386	0.0214	0.0428	0.0009	269.9	5.4
AHTL-14	444.02	699.12	0.64	0.3268	0.0188	0.0452	0.0008	284.7	5.0
AHTL-15	389.34	581.77	0.67	0.3245	0.0228	0.0454	0.0009	286.1	5.4
AHTL-16	857.76	1270.99	0.67	0.3408	0.0190	0.0454	0.0011	286.2	6.6
AHTL-17	380.83	613.47	0.62	0.3202	0.0275	0.0432	0.0009	272.5	5.3
AHTL-18	387.28	651.93	0.59	0.3379	0.0236	0.0460	0.0010	289.8	6.1
* AHTL-19	679.26	980.13	0.69	0.3876	0.0204	0.0490	0.0012	308.3	7.1
AHTL-20	480.76	740.62	0.65	0.3274	0.0188	0.0434	0.0008	273.8	4.7

* does not include zircon U–Pb dating.

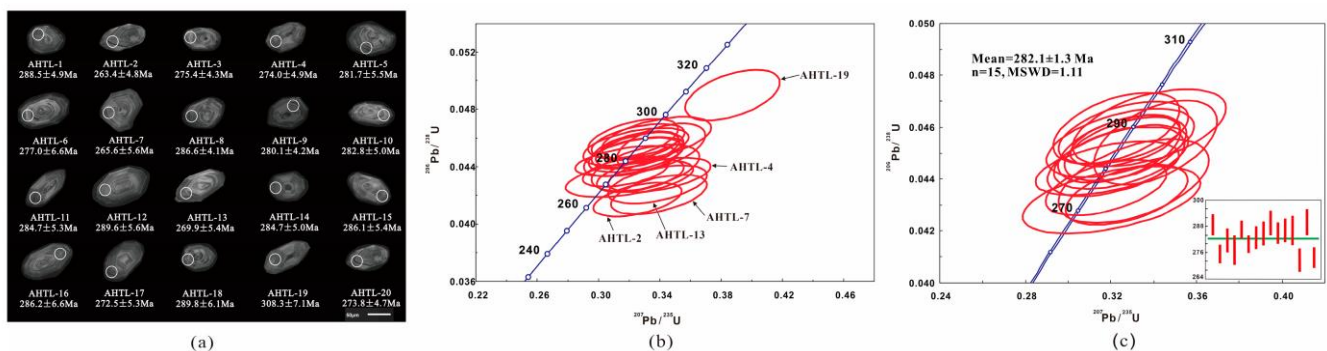


Figure 4. (a) Representative cathodoluminescence (CL) images of zircon grains; (b,c) ²⁰⁷Pb/²³⁵U–²⁰⁶Pb/²³⁸U concordia diagram and weighted average diagram of the Ahetala granodiorite.

5.2. Mineral Geochemistry

5.2.1. Plagioclase

As the main rock-forming mineral in Ahetala granodiorite, plagioclase can be used to study petrogenesis and magmatic evolution. The plagioclase samples show 56.47 to 58.78 wt.% for SiO₂; 24.69 to 26.14 wt.% for Al₂O₃; 6.88 to 8.43 wt.% for CaO; 7.00 to 7.82 wt.% for Na₂O; 31.66 to 38.84% for the An (anorthite) end-member; 58.36 to 65.11% for the Ab (albite) end-member; and 2.31 to 4.00% for the Or (orthoclase) end-member (Table 2). In the plagioclase, the An end-member is decreases and Ab end-member increases from core to rim (Figure 5a). The core is enriched in alkali, and the rim is enriched in acid.

Table 2. EPMA of plagioclase from Ahetala granodiorite.

Sample No.	AHTL-P11	AHTL-P12	AHTL-P13	AHTL-P14	AHTL-P15	AHTL-P16	AHTL-P17	AHTL-P18
	Oxides (wt.%)							
	Core				Rim			
SiO ₂	56.91	56.47	57.42	58.68	58.04	58.42	58.78	58.67
TiO ₂	0.08	-	0.01	0.10	0.16	-	-	0.20
Al ₂ O ₃	25.92	26.14	25.72	25.19	25.19	24.78	25.03	24.69
TFeO	0.28	0.24	0.15	0.20	0.13	0.24	0.26	0.25
MnO	-	0.05	0.12	-	0.05	0.22	-	-
MgO	-	-	-	-	-	0.01	-	0.06
CaO	8.43	8.40	8.07	7.19	7.39	7.01	6.99	6.88
Na ₂ O	7.00	7.06	7.23	7.81	7.56	7.64	7.65	7.82
K ₂ O	0.51	0.42	0.47	0.55	0.55	0.73	0.70	0.59
BaO	0.26	0.32	0.41	-	-	0.12	0.17	-
Σ	99.39	99.10	99.60	99.72	99.07	99.17	99.58	99.16
Structural formulae (a.p.f.u.) based on 8 oxygen atoms								
Si	2.59	2.58	2.60	2.64	2.64	2.65	2.65	2.66
Al	1.39	1.41	1.37	1.34	1.35	1.33	1.33	1.32
Ca	0.41	0.41	0.39	0.35	0.36	0.34	0.34	0.33
Na	0.62	0.62	0.64	0.68	0.67	0.67	0.67	0.69
K	0.03	0.02	0.03	0.03	0.03	0.04	0.04	0.03
Ba	0.01	0.01	0.01	0.00	0.00	0.00	0.01	0.00
End-members (%)								
An	38.84	38.75	37.17	32.72	34.02	32.30	32.26	31.66
Ab	58.36	58.94	60.26	64.31	62.97	63.70	63.89	65.11
Or	2.80	2.31	2.58	2.98	3.01	4.00	3.85	3.23

“-” indicates that the detection limit is not reached, the same as below.

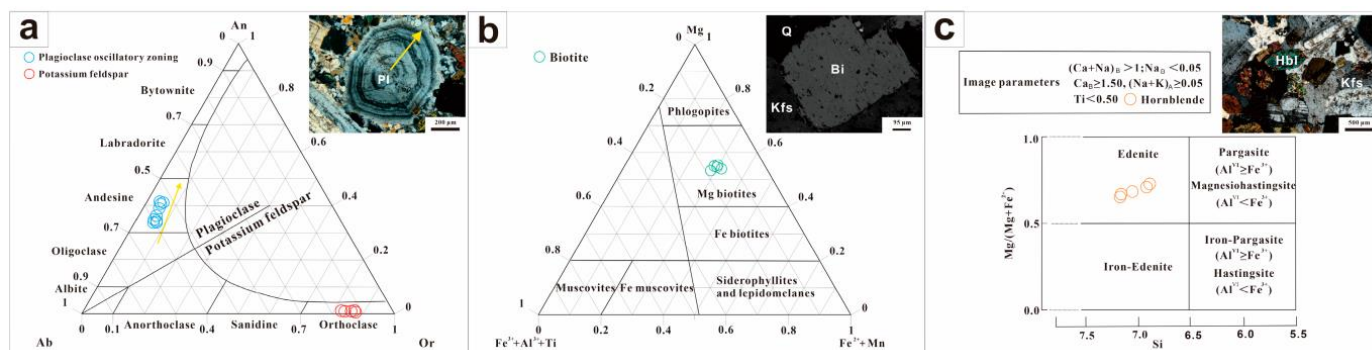


Figure 5. (a) Microscopic photograph of plagioclase (Bar = 200 μm) and classification graph of feldspar [59]; (b) back scattered electron (BSE) photograph and classification graph of biotite (Bar = 95 μm) [60]; (c) microscopic photograph and classification diagram of hornblende (Bar = 500 μm) [61]. Pl—Plagioclase; Q—Quartz; Kfs—Potassium feldspar; Bi—Biotite; Hbl—Hornblende.

5.2.2. Potassium Feldspar

The potassium feldspar samples show 62.32 to 63.24 wt.% for SiO₂; 19.05 to 19.57 wt.% for Al₂O₃; 13.48 to 13.82 wt.% for K₂O; 0.44 to 1.30% for An; 21.10 to 21.79% for Ab; and 77.50 to 78.43% for Or (Table 3). All potassium feldspar is orthoclase (Figure 5a).

Table 3. EPMA of potassium feldspar from Ahetala granodiorite.

Sample No.	AHTL-Kfs1	AHTL-Kfs2	AHTL-Kfs3	AHTL-Kfs4	AHTL-Kfs5
Oxides (wt.%)					
SiO ₂	62.34	63.08	62.76	63.24	62.32
TiO ₂	1.19	1.07	0.64	0.83	1.02
Al ₂ O ₃	19.29	19.29	19.05	19.25	19.57
TFeO	0.10	0.19	0.22	0.16	0.05
MnO	0.10	0.07	0.01	0.05	0.17
MgO	-	0.03	0.04	-	0.04
CaO	0.13	0.09	0.11	0.17	0.27
Na ₂ O	2.49	2.39	2.55	2.49	2.43
K ₂ O	13.51	13.48	13.82	13.53	13.58
Σ	99.14	99.69	99.20	99.72	99.45
Structural formulae (a.p.f.u.) based on 8 oxygen atoms					
Si	2.93	2.95	2.94	2.95	2.92
Al	1.07	1.06	1.05	1.06	1.08
Ca	0.01	0.01	0.01	0.01	0.01
Na	0.23	0.22	0.23	0.23	0.22
K	0.81	0.80	0.83	0.80	0.81
End-members (%)					
An	0.63	0.44	0.52	0.82	1.30
Ab	21.74	21.13	21.79	21.68	21.10
Or	77.63	78.43	77.69	77.50	77.60

5.2.3. Biotite

The biotite samples show 35.52 to 36.25 wt.% for SiO₂; 14.77 to 14.91 wt.% for Al₂O₃; 15.52 to 16.22 wt.% for TFeO; and 13.42 to 14.16 wt.% for MgO (Table 4). The biotite in Ahetala granodiorite belongs to magnesium biotite (Figure 5b).

Table 4. EPMA of biotite in Ahetala granodiorite.

Sample No.	AHTL-Bi1	AHTL-Bi2	AHTL-Bi3	AHTL-Bi4	AHTL-Bi5
Oxides (wt.%)					
SiO ₂	36.08	36.25	35.80	35.52	36.03
TiO ₂	4.10	4.42	4.43	4.30	4.50
Al ₂ O ₃	14.79	14.81	14.81	14.91	14.77
TFeO	15.77	15.62	15.69	16.22	15.52
MnO	0.23	0.33	0.31	0.04	0.21
MgO	14.16	14.12	13.97	13.71	13.42
CaO	0.13	0.04	0.02	-	0.05
Na ₂ O	0.37	0.38	0.37	0.53	0.40
K ₂ O	9.25	9.17	9.27	9.33	9.18
Σ	94.88	95.14	94.67	94.56	94.08
Structural formulae (a.p.f.u.) based on 11 oxygen atoms					
Si	2.73	2.73	2.72	2.71	2.74
Al ^{IV}	1.27	1.27	1.28	1.29	1.26
Al ^{VI}	0.05	0.05	0.04	0.05	0.07
Ti	0.23	0.25	0.25	0.25	0.26
Fe ³⁺	0.15	0.17	0.16	0.13	0.19
Fe ²⁺	0.85	0.81	0.84	0.90	0.80
Mn	0.01	0.02	0.02	0.00	0.01
Mg	1.60	1.59	1.58	1.56	1.52
Ca	0.01	0.00	0.00	0.00	0.00
Na	0.05	0.06	0.05	0.08	0.06
K	0.89	0.88	0.90	0.91	0.89
MF	0.61	0.61	0.61	0.60	0.60
Al ^{VI} + Fe ³⁺ + Ti	0.43	0.47	0.45	0.42	0.52
Fe ²⁺ + Mn	0.86	0.83	0.86	0.91	0.81

5.2.4. Hornblende

The hornblende of granodiorite samples show 46.05 to 48.63 wt.% for SiO₂; 5.69 to 7.80 wt.% for Al₂O₃; 13.08 to 14.23 wt.% for TFeO; 13.89 to 15.49 wt.% for MgO; and 11.27 to 11.56 wt.% for CaO (Table 5). All hornblende in granodiorite belongs to the edenite group (Figure 5c).

Table 5. EPMA of hornblende in Ahetala granodiorite.

Sample No.	AHTL-Hbl1	AHTL-Hbl2	AHTL-Hbl3	AHTL-Hbl4	AHTL-Hbl5
Oxides (wt.%)					
SiO ₂	48.63	48.15	46.99	46.18	46.05
TiO ₂	1.07	1.07	1.09	1.29	1.31
Al ₂ O ₃	5.69	6.15	6.94	7.80	7.56
TFeO	13.08	13.22	13.41	14.23	13.84
MnO	0.30	0.28	0.49	0.44	0.37
MgO	15.49	14.91	14.75	13.89	14.25
CaO	11.56	11.52	11.33	11.43	11.27
Na ₂ O	1.40	1.56	1.73	1.73	1.74
K ₂ O	0.51	0.58	0.64	0.79	0.68
Σ	97.73	97.44	97.37	97.78	97.07
Structural formulae (a.p.f.u.) based on 23 oxygen atoms					
Si	7.11	7.08	6.94	6.83	6.84
Al ^{IV}	0.89	0.92	1.06	1.17	1.16
Al ^{VI}	0.09	0.14	0.15	0.19	0.17
Ti	0.12	0.12	0.12	0.14	0.15
Fe ³⁺	0.47	0.45	0.36	0.33	0.34
Fe ²⁺	1.13	1.18	1.30	1.43	1.38
Mn	0.04	0.03	0.06	0.06	0.05
Mg	3.38	3.27	3.25	3.06	3.16
Ca	1.81	1.81	1.79	1.81	1.79
Na	0.40	0.44	0.50	0.50	0.50
K	0.10	0.11	0.12	0.15	0.13
Σ	15.53	15.55	15.64	15.67	15.66
Si _T	7.11	7.08	6.94	6.83	6.84
Al _T	0.89	0.92	1.06	1.17	1.16
Al _C	0.09	0.14	0.15	0.19	0.17
Fe ³⁺ _C	0.47	0.45	0.36	0.33	0.34
Ti _C	0.12	0.12	0.12	0.14	0.15
Mg _C	3.38	3.27	3.25	3.06	3.16
Fe ²⁺ _C	0.94	1.03	1.13	1.27	1.19
Mn _C	0.00	0.00	0.00	0.00	0.00
Fe ²⁺ _B	0.19	0.15	0.17	0.16	0.19
Mn _B	0.04	0.03	0.06	0.06	0.05
Ca _B	1.78	1.81	1.77	1.79	1.76
Na _B	0.00	0.00	0.00	0.00	0.00
Ca _A	0.03	0.00	0.03	0.02	0.03
Na _A	0.40	0.44	0.50	0.50	0.50
K _A	0.10	0.11	0.12	0.15	0.13
M	0.75	0.73	0.71	0.68	0.70

5.3. Whole-Rock Geochemistry

The results of major, trace and rare earth elements of five samples are listed in Table 6.

Table 6. Major (in wt%), trace and rare earth element (in ppm) compositions of Ahetala granodiorite.

Sample No.	AHTL-1	AHTL-2	AHTL-6	AHTL-7	AHTL-8
SiO ₂	62.35	63.66	61.69	62.74	62.63
TiO ₂	0.56	0.54	0.58	0.53	0.55
Al ₂ O ₃	15.95	15.67	16.29	15.45	15.78
TFe ₂ O ₃	4.78	4.75	4.84	4.59	4.89
MnO	0.05	0.07	0.06	0.06	0.07
MgO	3.26	3.30	3.39	3.28	3.42
CaO	4.64	4.65	4.88	4.70	4.79
Na ₂ O	4.11	3.72	4.08	3.65	3.73
K ₂ O	2.82	3.32	3.05	3.15	3.31
P ₂ O ₅	0.24	0.22	0.28	0.16	0.22
LOI	0.92	0.52	0.69	0.70	0.42
total	99.68	100.42	99.83	99.01	99.81
Na ₂ O + K ₂ O	6.93	7.04	7.13	6.80	7.04
A/NK	1.62	1.61	1.63	1.64	1.62
A/CNK	0.87	0.86	0.86	0.86	0.86
Mg#	54.87	55.33	55.53	56.02	55.49
DI	65.83	66.41	64.85	65.85	65.29
Ti	3482	3532	3866	3472	3506
Ga	17.044	17.584	18.902	17.490	14.570
Rb	80	123	96	105	32
Sr	767	723	829	708	481
Zr	221	222	214	216	209
Nb	14	16	17	15	15
Cs	3.182	4.984	3.444	3.096	3.586
Ba	1130	1077	1362	1089	567
La	30	38	40	42	13
Ce	62	68	80	74	36
Pr	7.376	7.424	9.074	7.764	3.766
Nd	27	25	32	26	14
Sm	4.636	4.202	5.220	4.242	2.626
Eu	1.345	1.243	1.539	1.245	0.790
Gd	3.876	3.560	4.364	3.586	2.240
Tb	0.540	0.490	0.597	0.490	0.343
Dy	3.016	2.770	3.290	2.756	1.971
Ho	0.629	0.580	0.687	0.576	0.427
Er	1.752	1.616	1.917	1.603	1.218
Tm	0.256	0.244	0.286	0.241	0.184
Yb	1.721	1.622	1.843	1.613	1.242
Lu	0.267	0.263	0.285	0.261	0.198
Hf	5.612	5.611	5.362	5.369	5.274
Ta	0.798	1.260	1.277	1.397	1.006
Pb	25.200	22.860	25.060	19.826	19.358
Th	10.932	18.064	13.408	20.460	5.142
U	1.914	3.530	2.168	3.404	1.829
ΣREE	144.35	155.47	180.28	165.64	78.42
LREE	132.30	144.33	167.01	154.51	70.60
HREE	12.06	11.14	13.27	11.13	7.82
LREE/HREE	10.97	12.95	12.59	13.89	9.02
(La/Yb) _N	12.68	16.82	15.54	18.60	7.53
δEu	0.94	0.96	0.96	0.95	0.97
δCe	0.98	0.94	0.98	0.93	1.26
Yb + Nb	16.16	17.52	18.36	16.94	16.49
Nb/Ta	18.10	12.62	12.93	10.97	15.16
Zr/Hf	39.41	39.64	39.95	40.19	39.59
La/Yb	17.68	23.45	21.67	25.93	10.50
Th/Nd	0.41	0.72	0.42	0.79	0.37
La/Sm	6.56	9.05	7.65	9.86	4.97
Th/U	5.71	5.12	6.18	6.01	2.81
Rb/Sr	0.10	0.17	0.12	0.15	0.07

5.3.1. Major Elements

The Ahetala granodiorite samples show 61.69 to 63.66 wt.% for SiO₂; 3.26 to 3.42 wt.% for MgO; 0.16 to 0.28 wt.% for P₂O₅; 3.65 to 4.11 wt.% for Na₂O; and 2.82 to 3.32 wt.% for K₂O. All the samples have a high content of K₂O + Na₂O (6.80–7.13 wt.%) and relatively low A/CNK ratios (0.86–0.87) (Table 6), indicating a calc-alkaline, metaluminous affinity. Granodiorite has low TFe₂O₃/MgO ratios (1.40–1.47) and high Mg# values (54.87–56.02) (Mg# = 100 × Mg/(Mg + Fe²⁺)).

All the samples in the SiO₂ vs. Na₂O-K₂O diagram belong to granodiorite (Figure 6a). The results are consistent with the Q-A-P diagram of intrusive rocks and petrographic observations. In A/NK vs. A/CNK diagram, all the studied samples are plotted in the metaluminous field (Figure 6b). All the samples are plotted in the field of high-k calc-alkaline in the SiO₂ vs. K₂O diagram (Figure 6c). To sum up, Ahetala granodiorite belongs to high-K calc-alkaline granite.

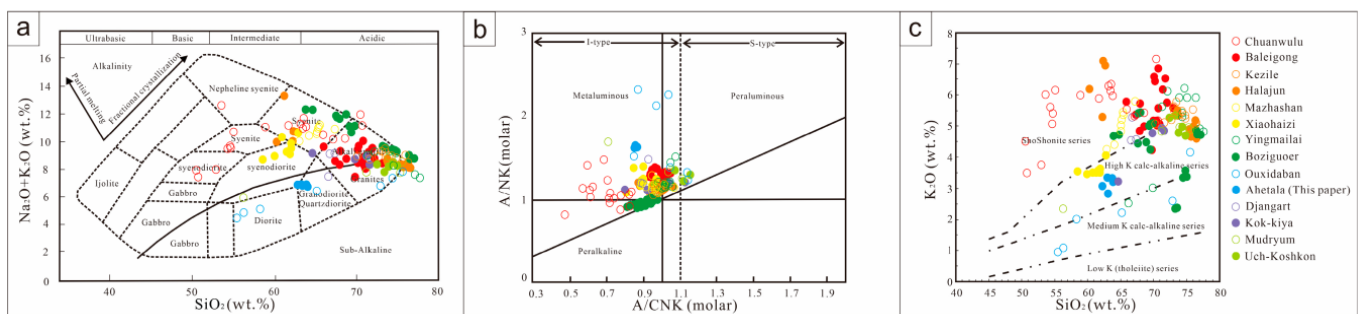


Figure 6. (a) TAS diagram [62]; (b) A/NK vs. A/CNK diagram [63] (A/CNK = Al₂O₃/(CaO + Na₂O + K₂O) molar, A/NK = Al₂O₃/(Na₂O + K₂O) molar); (c) K₂O vs. SiO₂ diagram [64]. Data sources: Chuanwulu [25]; Baleigong [26,27]; Kezile and Halajun [29,42]; Mazhashan [43]; Xiaohaizi [44]; Yingmailai [38,45]; Boziguoer [46]; Oxidaban [47]; Djangart, Kok-kiya, Mudryum, and Uchkoshkon [48–51]; Ahetala (this paper), as in figures in Sections 6.1.1 and 6.2.

5.3.2. Trace Elements

The primitive mantle normalized trace element diagrams show that the Ahetala granodiorite is relatively enriched in large ionic lithophile elements (LILEs), such as K, Sr, and Ba, and relatively depleted in high field strength elements (HFSEs), such as Nb, Ta, and Ti (Figure 7a). Yb + Nb range from 16.16 to 18.36; Nb/Ta range from 10.97 to 18.10; Rb/Sr range from 0.07 to 0.17; and Zr/Hf range from 39.41 to 40.19 (Table 6).

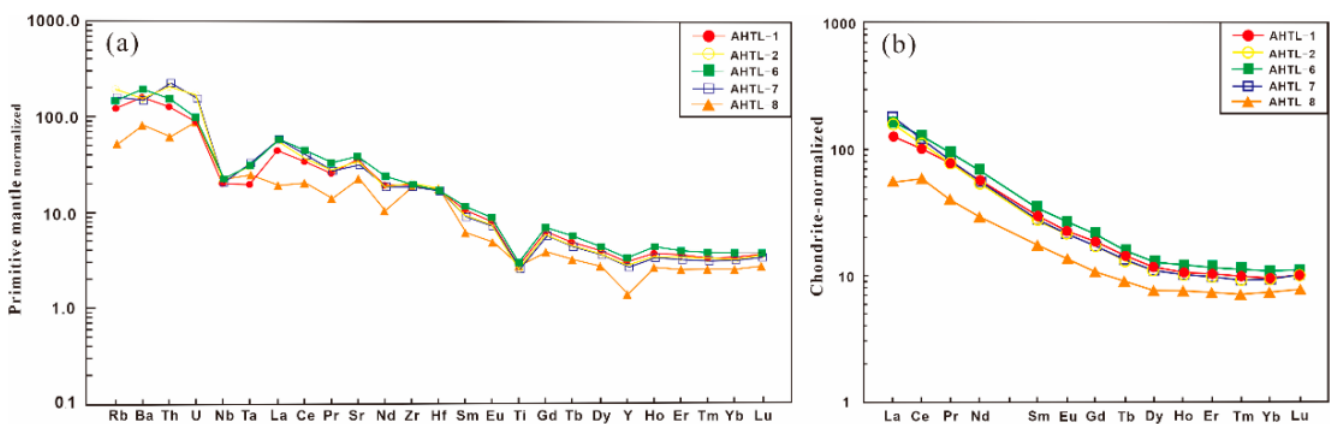


Figure 7. (a) Primitive mantle-normalized spidergrams for Ahetala granodiorite; (b) chondrite-normalized REE patterns for Ahetala granodiorite. The normalized values are from [65].

The total rare earth elements (ΣREE) of Ahetala granodiorite concentrations range from 78.42 to 180.28 ppm with an average of 144.83 ppm. The contents of light rare earth

elements (LREE) are between 70.60 to 167.01 ppm with an average of 133.75 ppm. The contents of heavy rare earth elements (HREE) are between 7.82 to 13.27 ppm with an average of 11.08 ppm. The LREE/HREE ranging from 9.02 to 13.89. LREE are enriched relative to HREE in the chondrite-normalized REE diagram (Figure 7b) with $(La/Yb)_N$ ratios ranging from 7.53 to 18.60. The distribution of rare earth elements is a standard right-leaning pattern, and HREE display a relatively flat distribution pattern. The negative Eu anomaly is not obvious ($\delta Eu = 0.94\text{--}0.97$) and is likely affected by the fractionation of plagioclase during the magmatic evolution.

6. Discussion

6.1. Petrogenesis

6.1.1. Geochemical Affinities

All studied samples belong to granodiorite in the TAS diagram (Figure 6a), consistent with petrographic observations. All of the samples are enriched in the K and calc-alkaline series (Figure 6c), which are different from M-type granites that have low K (<1%) [66]. Further, the Ahetala granodiorite belongs to the high-K series (Figure 6c) and has low Nb contents, 10,000 Ga/Al ratios (Figure 8a), TFeO/MgO ratios, Zr+Ce+Y+Nb contents (Figure 8b), and K_2O+Na_2O/CaO ratios, which preclude them from A-type granite [67–69]. Ahetala granodiorite is characterized by low differentiation indices ($DI = 64.85\text{--}66.41$) and is plotted in the field of unfractionated I-, S-, and M-type granites (Figure 8a,b). S-type granites generally have aluminum-rich minerals, such as cordierite, muscovite, tourmaline, and garnet [70]. However, mineralogical observation did not find these minerals in Ahetala granodiorite. The MF value of biotite ($MF = [Mg/(Mg + Fe + Mn)]$) can also be used to distinguish S-type and I-type granite (S-type granite < 0.5, I-type granite > 0.5 [71]). The MF value of Ahetala granodiorite is ~0.6, thus showing the characteristics of I-type granite.

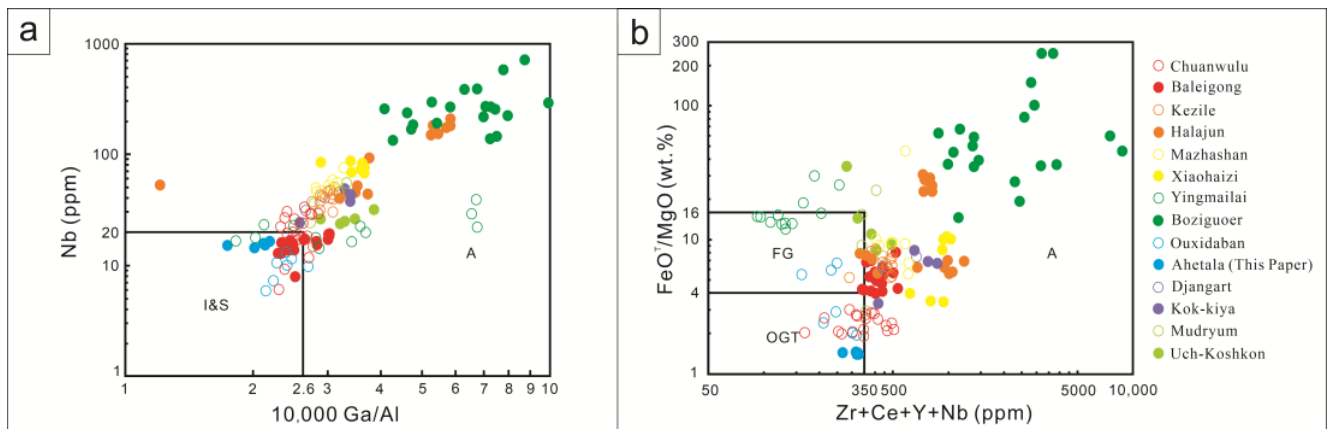


Figure 8. (a) 10,000 Ga/Al vs. Nb and (b) Zr+Ce+Y+Nb vs. TFeO+MgO [68]. I = I-type; S = S-type; M = M-type granite; FG = fractionated felsic granites; OGT = unfractionated I-, S-, and M-type granites.

In addition, the low A/CNK ratios, the negative correlation between P_2O_5 and SiO_2 (Figure 9a), and the positive correlation between Rb and Th, Rb, and Y (Figure 9b,c) indicate the petrogenesis of I-type granites and preclude Ahetala granodiorite from being S-type granite [72,73]. In summary, our petrographic observations and geochemical evidence suggest that Ahetala granodiorite is I-type granite.

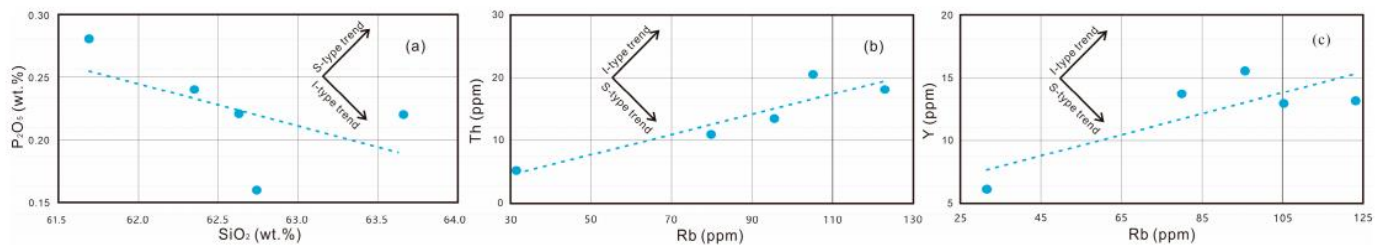


Figure 9. (a) SiO₂-P₂O₅ diagram; (b) Rb-Th diagram; and (c) Rb-Y diagram [72].

6.1.2. Magma Source

Geochemically, the electron probe microanalysis of rock-forming minerals is helpful when analyzing the magmatic source. The An contents of plagioclase decreases with fluctuation from the core to rim, which shows the characteristics of a normal zoning, indicating that the plagioclase was directly formed by the crystallization of mixed magma [74]. The MgO content of biotite from the crust is usually lower than 6 wt.%, while that from the mantle is generally higher than 15% [75,76]. The MgO content of biotites in all the samples is 13.42–14.16 wt.%, which reflects the characteristics of a crust–mantle mixed source (Table 4). In addition, the M value ($M = \text{Mg}/(\text{Mg} + \text{Fe}^{2+})$) of amphiboles can also be used to distinguish the magmatic source [77]. The M value of all amphiboles ranging between 0.68 and 0.75 ($0.5 < M < 0.7$ for crust–mantle type granite and $M > 0.7$ for mantle type granite) indicates that Ahetala granodiorite has the characteristics of the crust–mantle mixed source. The TFeO/(TFeO + MgO) vs. MgO diagram (Figure 10a) shows that all biotites belong to crust–mantle mixed sources [78]. In the Al₂O₃ vs. TiO₂ diagram, all amphiboles are plotted in the field of the crust–mantle mixed source (Figure 10b). The Nb/Ta ratios of Ahetala granodiorite (10.97–18.10) are similar to those of the crust (~11–12) and mantle (~17.5) [79], indicating that granodiorite is of crust–mantle mixed origin. The Zr/Hf ratios of Ahetala granodiorite (39.41–40.19) are similar to the value of MORB (~36) [65], indicating that mantle-derived material may indeed be involved in magmatic evolution. The Th/U ratios of granodiorite ranging from 2.81 to 6.18 (average of 5.17), which are similar to the lower crust (Th/U = 5.48) [80,81]. Previous studies have shown that magmas with Mg# > 40 are related to the involvement of a mantle component [82], which is consistent with the Mg# (54.87–56.02) of the Ahetala granodiorite. The SiO₂ (61.69%–63.66%) and Al₂O₃ (15.45%–16.29%) values; enriched Zr and Hf; and depleted Nb, Ta, and Ti in samples indicate that mantle-derived materials contribute to magmatic evolution [83].

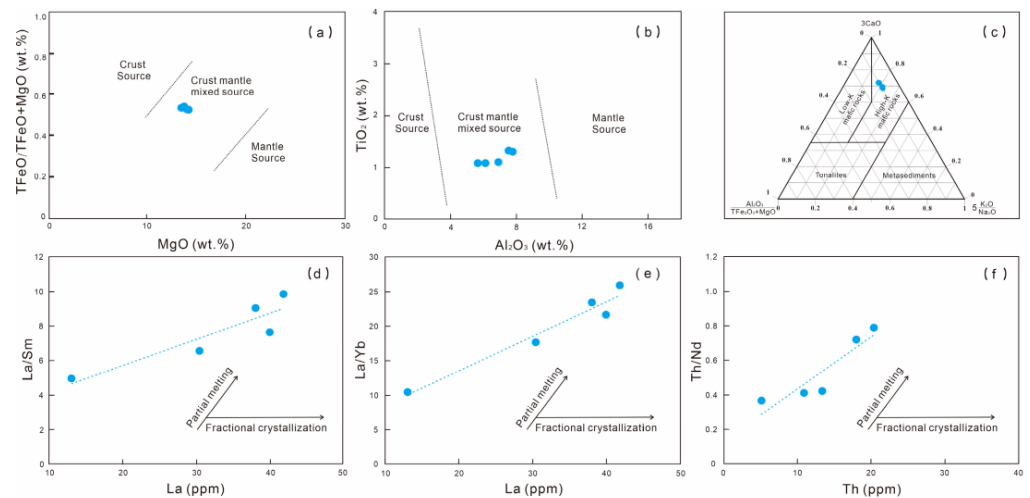


Figure 10. (a) The w(MgO)% vs. w(TFeO)/w(TFeO + MgO)% diagram for the biotites [78]; (b) the w(TiO₂)% vs. w(Al₂O₃)% diagram for the amphiboles [85]; (c) the Al₂O₃/ (TFe₂O₃ + MgO) – 3 × CaO – 5 × (K₂O/Na₂O) diagram for the granitoid [84]; (d) La vs. La/Sm and (e) La vs. La/Yb [86]; (f) the Th vs. Th/Nd diagram [87].

In addition to the above characteristics, all the plotted samples fall within the field of high-K mafic rocks (Figure 10c), which indicates that the magma may originate from the mafic magmas [84]. Similarly, Ahetala granodiorite shows an obvious tendency towards partial melting (Figure 10d–f). The above geochemical features indicates that the Ahetala granodiorite is mainly generated from the crustal contamination of the mantle-derived mafic magmas.

6.2. Emplacement Age and Tectonic Setting

The STOB is widely accepted as a Paleozoic collision belt formed by the collision of the Tarim Craton and Yili-Central Tianshan block. It has undergone subduction, accretion, collision, crust thickening, and extension-thinning [10,34,35]. However, direct geological evidence of the evolutionary process of STOB was almost eradicated in the subsequent geological evolution. Therefore, it is difficult to infer the evolutionary process of the STO, resulting in controversy about the closing time of the STO and the tectonic setting of the Permian in south Tianshan. Some studies have proposed that the STO was a post-collision setting in the Early Permian (the closure of the STO occurred before the Early Permian) [35,54]. In contrast, others believe it is a volcanic arc setting related to subduction (the closure of the STO occurred in or after the Early Permian) [15,23]. The formation time of tectonic suture belt can be constrained through the youngest ophiolite and the earliest pluton or dikes intruding into the suture belt [13]. Previous studies have shown that the age of the south Tianshan ophiolite belt is 450 Ma to 392 Ma, and these ophiolites belong to supra-subduction zone (SSZ) type ophiolites [17–19], which suggests that the south Tianshan oceanic crust had existed since the Silurian. Liu Bin et al. measured the Ar–Ar age (360 Ma) of the glaucophane in the Kumishi area, which indicates a northward subduction of the south Tianshan oceanic crust [88].

High-pressure/ultra-high pressure (HP-UHP) metamorphic belts in the STOB were considered to be the product of the collision between the Tarim Craton and the Yili-Central Tianshan plate [12,89]. Previous studies on the HP metamorphism have shown that the Late Carboniferous (320 Ma) is the initial collision and the upper age limit is 285 Ma [10]. Radiolarian fossils were discovered in the accretionary complex, which confirmed that the relic ancient oceanic basin existed in the western part of the STO during the Early Permian [23]. In the high-pressure metamorphic zone of the northern part of the STOB, the zircon ages of granulite range from 290 to 280 Ma, indicating that subduction finished in the STO during the Early Permian [90].

As shown in Figure 4, the result indicates that the age of granodiorite is 282.1 ± 1.3 Ma ($n = 15$, MSWD = 1.11), which reflects that granodiorite was emplaced in the Permian. This age is consistent with the emplacement time of granitic rocks in the Kokshal mountains (273–283 Ma) [91]. By studying the Paleozoic granites in the STOB, a large number of studies believe that the STOB was in a critical period of transition from the subduction to collision during the Late Carboniferous to the Early Permian [2].

All samples of Ahetala granodiorite plotted in the field of volcanic arc granites (VAG), syn-collision granites (syn-COLG), and post-collision granites (post-COLG) in the Y vs. Nb and Y + Nb vs. Rb diagrams (Figure 11a,b). In the R_1 vs. R_2 diagram, all samples plotted on the boundary between the pre-plate collision and post-collision uplift (Figure 11c). Three samples are plotted in the field of VAG, while the other two are plotted in the field of the late to post-orogenic calc-alkaline intrusions (COLG III) and within plate granites (WPG) in the $3\text{Ta-Rb}/30\text{-Hf}$ diagram (Figure 11d). In the $Y/15\text{-La}/10\text{-Nb}/8$ diagram, four samples are plotted on the boundary of the orogenic domains and late to post orogenic field and one sample is plotted in the late to post orogenic field (Figure 11e). In addition, biotites belong to calc-alkaline subduction-related biotites in the $\text{TFeO-MgO-Al}_2\text{O}_3$ discriminant diagram (Figure 11f) [92]. The enrichment of K, LREEs, and LILEs and the depletion in HFSE (Figure 7b) and minor Eu anomalies ($\delta\text{Eu} = 0.94\text{--}0.97$) are signatures characteristically associated with subduction-related magmas [93]. Meanwhile, the negative anomalies of Nb, Ta, and Ti can be found in the primitive mantle-normalized spidergrams, which

also indicate that Ahetala granodiorite has the characteristics of arc granites (Figure 7a). However, it is difficult to distinguish between tectonic settings using tectonic discrimination diagrams because they often reach ambiguous conclusions. Nevertheless, it is indisputable that the crust thickens due to the extrusion and collision in the collisional stage. High potassium granite implies crustal thickening after collision [50,94]. In addition, as described in Section 6.1.2, under the dynamic background of subduction and collision, the underplating of the mantle material is considered to be the main factor of crustal thickening [95]. It is only during this period that mantle-derived materials may participate in the magmatic evolution.

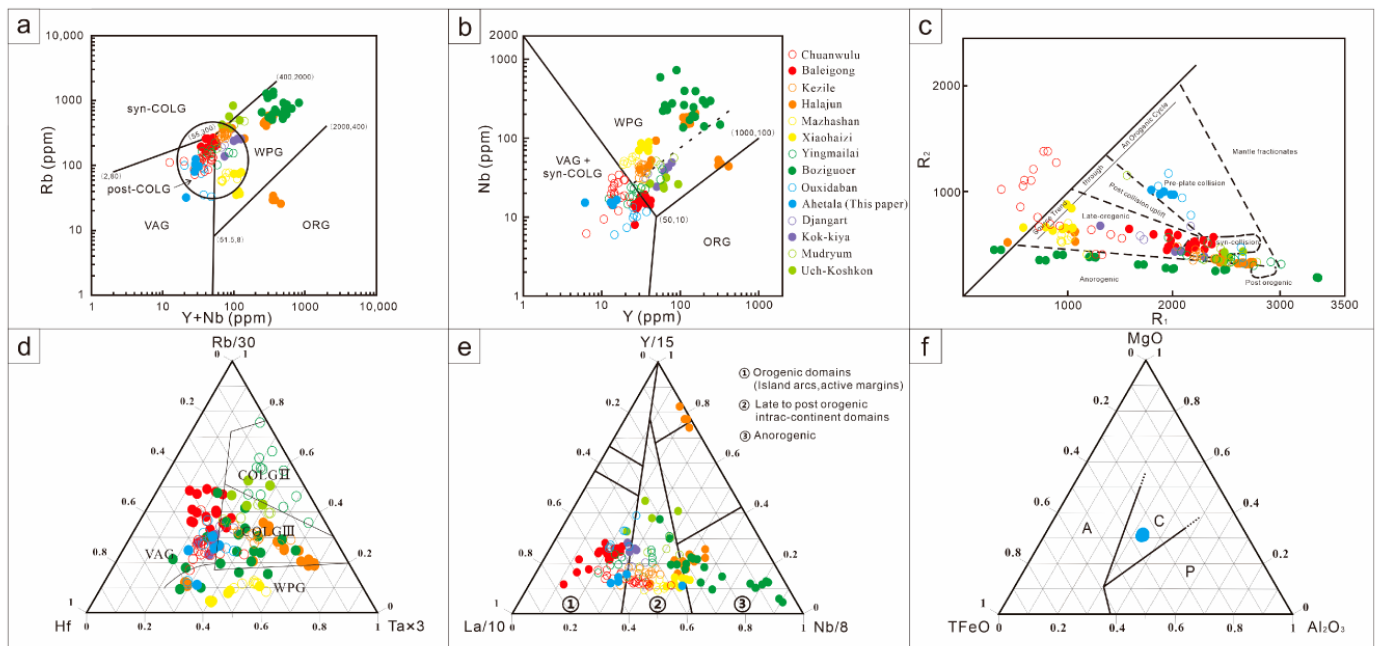


Figure 11. (a) Y + Nb vs. Rb diagram; (b) Y vs. Nb diagram [96] (syn-COLG = syn-collision granites, VAG = volcanic arc granites, WPG = within plate granites, ORG = ocean ridge granites, post-COLG = post-collision granites); (c) R_1 vs. R_2 diagram [97] ($R_1 = 4Si - 11(Na + K) - 2(Fe + Ti)$, $R_2 = Al + 2Mg + 6Ca$); (d) Rb/30-Hf-3Ta diagram [98]; (e) Y/15-La/10-Nb/8 diagram [93]; (f) TFeO-Al₂O₃-MgO diagram (A: anorogenic alkaline suites; C: calc-alkaline subduction-related suites; P: peraluminous (including S-type) suites) [92].

Therefore, according to the restriction of the geochemical affinities, magma source, and the multiple tectonic discrimination diagrams, the formation setting of Ahetala granodiorite is the transitional stage of the volcanic arc (syn-collision) and post-collision setting. This means that the STO in this region was closed in the Early Permian (282.1 ± 1.3 Ma).

6.3. Implication for the Tectonic Evolution of the STO

Many granitic rocks of the Late Carboniferan–Early Permian have been studied in STOB, and fruitful data have been accumulated. However, the tectonic evolution of the STOB in the Early Permian is still in debate, because it is not possible to determine the closing time of the STO only based on the evidence of the age and tectonic setting of such granites (most are A-type granites). These intrusions are almost evenly distributed in the STOB over more than 1500 km. No single granitic rock can prove the geodynamic setting of the whole STO in the Late Paleozoic.

Regarding the evolution of the STO in the Paleozoic, most studies argue that the south Tianshan oceanic crust subducted northward beneath the southern margin of the Yili-Central Tianshan plate during the Silurian to Middle Devonian [35,99,100]. Some previous studies believe that oblique collision played a vital role in the closing process of the STO in the late Paleozoic based on studies of large displacement strike-slip faults

and paleomagnetism data [99,101]. Other relevant studies argue that the remnant basin of STO gradually closed from east to west in a “scissors-like” collision during the Late Carboniferous to Early Permian [102,103]. In the late Devonian, the eastern part of the Tarim Craton had already collided with the Yili-Central Tianshan plate, leaving a west-facing remnant oceanic basin [99]. Only the final consumption of the remnant oceanic crust means the end of the collision.

We have collected the data of granitic rocks from the Late Carboniferous–Early Permian in the STOB (Table 7). Most are intermediate-acidic metaluminous magmatic rocks (Figure 6), belonging to WPG (A-type granites) and formed in the post-collision (extensional) setting (Figures 8 and 11). The age of these collision-related granites ranging from 261.5 ± 2.1 Ma to 304.2 ± 11.6 Ma, with an average of about 284.4 Ma (Figure 12). The ages of post-collision granites of the eastern part are older than the western part in the STOB. This finding means that the eastern part of STO developed into a post-collision setting earlier than the western part. When the AhetaIa granodiorite was formed (282.1 ± 1.3 Ma), the western segment of the STO was still in the transitional stage of the volcanic arc (syn-collision) and post-collision setting. This conclusion also demonstrates the possibility of a “scissors-like” collision of the STO.

Chen et al. also believe that the “scissors-like” collision of the Tarim Craton with the Yili-Central Tianshan plate gave rise to the lithosphere-scale strike-slip and formed the northern Tarim Early Permian magmatic arc [99]. This view is also consistent with the conclusion that AhetaIa granodiorites have the characteristics of volcanic arc granite and were formed during the transitional stage between the volcanic arc (syn-collision) and the post-collision setting. Combined with previous research and the nature of AhetaIa granodiorite, we believe that the western part of STO, where AhetaIa granodiorite is located, was closed in the Early Permian. The Tarim Craton and Yili-Central Tianshan plate were fully amalgamated in the Early Permian (Figure 13).

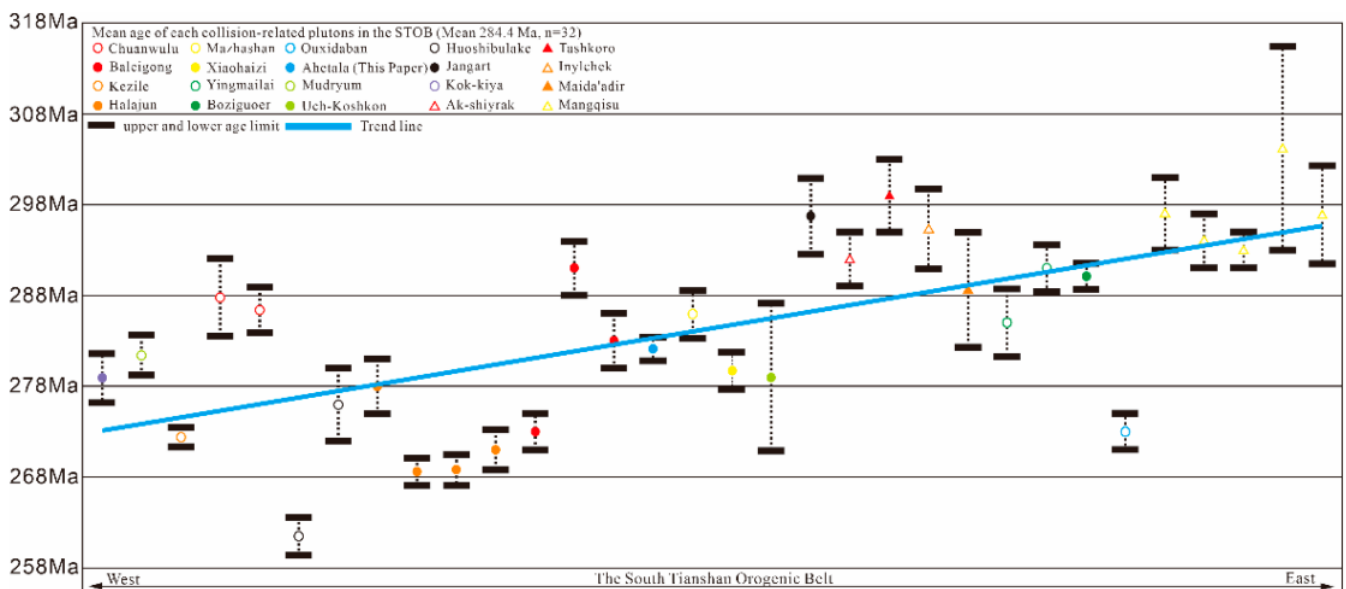


Figure 12. Distribution map of the age and geographic position of intrusions in the South Tianshan Orogenic Belt.

Table 7. Late Carboniferous to Early Permian collision-related granitic intrusions in the South Tianshan Orogenic Belt.

Pluton	Description	Method	Age	Type	Environment
Chuanwulu [25,45]	Biotite diorite Biotite monzonite	LA-ICP-MS	287.8 ± 4.3 Ma 286.4 ± 2.5 Ma	I	Post-collision
Baileigong [26,27]	Biotite moyite	LA-ICP-MS	273 ± 2 Ma 291 ± 3 Ma 283 ± 3 Ma	A2	Post-collision
Huoshibulake [28,29,45]	Alkali-feldspar granite	ID-TIMS SHRIMP	261.5 ± 2.7 Ma 276 ± 4 Ma	A1	Post-collision
Kezile [42]	Biotite granite	LA-ICP-MS	272.4 ± 1.1 Ma	A1	Post-collision
Halajun [29,42]	Granite Quartz syenite	SHRIMP LA-ICP-MS	278 ± 3 Ma 268.6 ± 1.5 Ma 268.8 ± 1.7 Ma 271.0 ± 2.2 Ma	A1	Post-collision
Mazhashan [43]	Syenite	SHRIMP	285.9 ± 2.6 Ma	A1	Post-collision
Xiaohaizi [44]	Syenite	SIMS	279.7 ± 2 Ma	A	Post-collision
Yingmailai [38,45]	Biotite monzonite granite	LA-ICP-MS	285.0 ± 3.7 Ma 291.0 ± 2.6 Ma	S	Syn-collision- Post-collision
Boziguoer [46]	Granite	LA-ICP-MS	290.1 ± 1.4 Ma	A	Post-collision
Oxidaban [47]	Monzonitic granite	LA-ICP-MS	273 ± 2 Ma	I	Pre-collision
Djangart [48–51]	Granite	SIMS	296.7 ± 4.2 Ma	A2	Post-collision
Uchkoshkon [48–51]	Granite	SIMS	279 ± 8.1 Ma	A2	Post-collision
Mudryum [48–51]	Granite	SIMS	281.4 ± 2.2 Ma	A2	Post-collision
Kok-kiya [48–51]	Granite	SIMS	278.9 ± 2.7 Ma	A2	Post-collision
Ak-Shiyrak [48–51]	Granite	SHRIMP	292 ± 3 Ma	A2	Post-collision
Tashkoro [48–51]	Granite	SHRIMP	299 ± 4 Ma	A	Post-collision
Inylchek [48–51]	Granite	SHRIMP	295.3 ± 4.4 Ma	A	Post-collision
Maida'adir [48–51]	Granite	SHRIMP	288.6 ± 6.3 Ma	A	Post-collision
Mangqisu [32,45,104]	Granodiorite	SHRIMP LA-ICP-MS	296.9 ± 5.4 Ma 304.2 ± 11.6 Ma 292 ± 2 Ma 297 ± 4 Ma 294 ± 3 Ma	I	Syn-collision-Post-collision

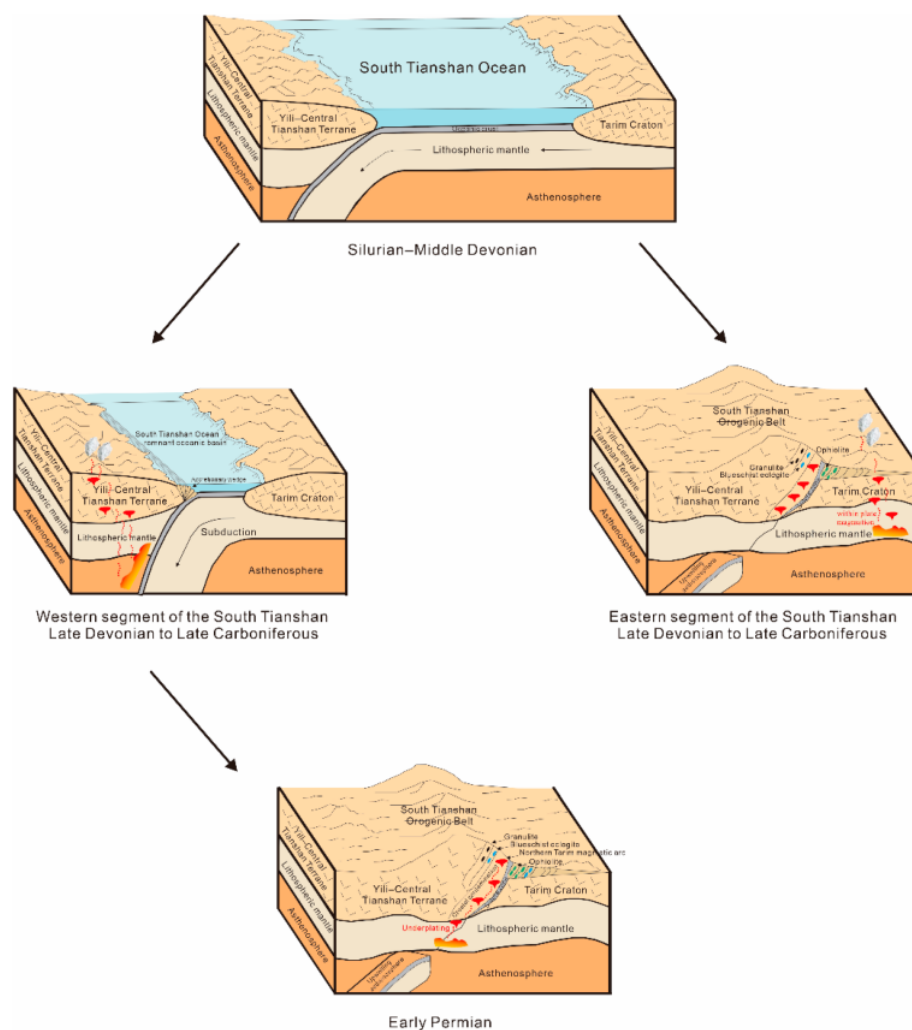


Figure 13. Tectonic evolutionary schematic diagram of the South Tianshan Ocean in the Paleozoic.

7. Conclusions

Based on experimental data of Ahetala granodiorite in this paper and previous research results on the Late Paleozoic tectonic evolution in the STOB, we reach the following conclusions:

1. The LA–ICP–MS U–Pb dating of zircons from Ahetala granodiorite yielded a precise crystallization age of 282.1 ± 1.3 Ma (MSWD = 1.11).
2. Ahetala granodiorite belongs to the high-K calc-alkaline series I-type granitoid.
3. Ahetala granodiorite was triggered by the crustal contamination of the mantle-derived magmas, which involved the mixing of crust- and mantle-derived materials.
4. Ahetala granodiorite was emplaced in the transitional stage of the volcanic arc (syn-collision) and the post-collision setting, indicating the STO was closed in the Early Permian.

Author Contributions: Conceptualization, Y.X. and J.Y.; investigation, J.Y., H.X., J.F. and M.F.; data curation, Y.X.; writing—original draft preparation, Y.X.; writing—review and editing, Y.X., J.Y. and C.W.; project administration, J.Y.; funding acquisition, J.Y. and K.X. All authors have read and agreed to the published version of the manuscript.

Funding: This research was supported by the National Key Technology Research and Development Program (2017YFC0601500).

Data Availability Statement: The experimental data used to support the conclusions of this study are included within the article.

Acknowledgments: Thanks to Jinhua Hao, Li Su, Wang Kunming, Shen Lijian, Yuwei Gao, Zhenhua Zhang, Fei Zhao, Piao Zhang, Yandong Sun, and other geologists and scholars for their guidance and help. Thanks to the editorial department for its valuable comments and suggestions for revision.

Conflicts of Interest: The authors declare no conflict of interest.

References

1. Dobretsov, N.L.; Berzin, N.A.; Buslov, M.M. Opening and Tectonic Evolution of the Paleo-Asian Ocean. *Int. Geol. Rev.* **1995**, *37*, 335–360. [\[CrossRef\]](#)
2. Windley, B.F.; Alexeiev, D.; Xiao, W.; Kröner, A.; Badarch, G. Tectonic Models for Accretion of the Central Asian Orogenic Belt. *J. Geol. Soc.* **2007**, *164*, 31–47. [\[CrossRef\]](#)
3. Jahn, B.; Wu, F.; Chen, B. Granitoids of the Central Asian Orogenic Belt and Continental Growth in the Phanerozoic. *Earth Environ. Sci. Trans. R. Soc. Edinb.* **2000**, *91*, 181–193. [\[CrossRef\]](#)
4. Kovalenko, V.I.; Yarmolyuk, V.V.; Kovach, V.P.; Kotov, A.B.; Kozakov, I.K.; Salnikova, E.B.; Larin, A.M. Isotope Provinces, Mechanisms of Generation and Sources of the Continental Crust in the Central Asian Mobile Belt: Geological and Isotopic Evidence. *J. Asian Earth Sci.* **2004**, *23*, 605–627. [\[CrossRef\]](#)
5. Sengör, A.M.C.; Natal'in, B.A.; Burtman, V.S. Evolution of the Altaid Tectonic Collage and Palaeozoic Crustal Growth in Eurasia. *Nature* **1993**, *364*, 299–307. [\[CrossRef\]](#)
6. Dobretsov, N.L.; Buslov, M.M.; Vernikovskiy, V.A. Neoproterozoic to Early Ordovician Evolution of the Paleo-Asian Ocean: Implications to the Break-up of Rodinia. *Gondwana Res.* **2003**, *6*, 143–159. [\[CrossRef\]](#)
7. Charvet, J.; Shu, L.S.; Laurent-Charvet, S. Paleozoic Structural and Geodynamic Evolution of Eastern Tianshan (NW China): Welding of the Tarim and Junggar Plates. *Epis. J. Int. Geosci.* **2007**, *13*, 162–186.
8. Charvet, J.; Shu, L.; Laurent-Charvet, S.; Wang, B.; Faure, M.; Cluzel, D.; Chen, Y.; De Jong, K. Palaeozoic Tectonic Evolution of the Tianshan Belt, NW China. *Sci. China Earth Sci.* **2011**, *54*, 166–184. [\[CrossRef\]](#)
9. Wang, B.; Faure, M.; Shu, L.; de Jong, K.; Charvet, J.; Cluzel, D.; Jahn, B.; Chen, Y.; Ruffet, G. Structural and Geochronological Study of High-Pressure Metamorphic Rocks in the Kekesu Section (Northwestern China): Implications for the Late Paleozoic Tectonics of the Southern Tianshan. *J. Geol.* **2010**, *118*, 59–77. [\[CrossRef\]](#)
10. Gao, J.; Klemd, R.; Qian, Q.; Zhang, X.; Li, J.; Jiang, T.; Yang, Y. The Collision between the Yili and Tarim Blocks of the Southwestern Altai: Geochemical and Age Constraints of a Leucogranite Dike Crosscutting the HP–LT Metamorphic Belt in the Chinese Tianshan Orogen. *Tectonophysics* **2011**, *499*, 118–131. [\[CrossRef\]](#)
11. Wang, B.; Shu, L.; Faure, M.; Jahn, B.; Cluzel, D.; Charvet, J.; Chung, S.; Meffre, S. Paleozoic Tectonics of the Southern Chinese Tianshan: Insights from Structural, Chronological and Geochemical Studies of the Heiyingshan Ophiolitic Mélange (NW China). *Tectonophysics* **2011**, *497*, 85–104. [\[CrossRef\]](#)
12. Gao, J.; Klemd, R.; Zhang, L.; Wang, Z.; Xiao, X. P-T Path of High-Pressure/Low-Temperature Rocks and Tectonic Implications in the Western Tianshan Mountains, NW China. *J. Metamorph Geol.* **1999**, *17*, 621–636. [\[CrossRef\]](#)
13. Han, B.; Guo, Z.; Zhang, Z.; Zhang, L.; Chen, J.; Song, B. Age, Geochemistry, and Tectonic Implications of a Late Paleozoic Stitching Pluton in the North Tian Shan Suture Zone, Western China. *Geol. Soc. Am. Bull.* **2010**, *122*, 627–640. [\[CrossRef\]](#)
14. Allen, M.B.; Windley, B.F.; Zhang, C. Palaeozoic Collisional Tectonics and Magmatism of the Chinese Tien Shan, Central Asia. *Tectonophysics* **1993**, *220*, 89–115. [\[CrossRef\]](#)
15. Xiao, W.; Windley, B.F.; Allen, M.B.; Han, C. Paleozoic Multiple Accretionary and Collisional Tectonics of the Chinese Tianshan Orogenic Collage. *Gondwana Res.* **2013**, *23*, 1316–1341. [\[CrossRef\]](#)
16. Zhao, Z.; Zhang, Z.; Santosh, M.; Huang, H.; Cheng, Z.; Ye, J. Early Paleozoic Magmatic Record from the Northern Margin of the Tarim Craton: Further Insights on the Evolution of the Central Asian Orogenic Belt. *Gondwana Res.* **2015**, *28*, 328–347. [\[CrossRef\]](#)
17. Wang, Y.; Huang, H.; Zhang, D.; Zhang, Z.; Encarnacion, J.; Zhao, L. SHRIMP Dating of the Qiqijianake Ophiolitic Mélange in the Kokshal Region, southwestern Tianshan and Its Tectonic Implications. *Acta Petrol. Sin.* **2012**, *28*, 328–347.
18. Wang, C.; Liu, L.; Che, Z.; Luo, J.; Zhang, J. Geochronology, Petrogenesis and Significance of Baleigong Mafic Rocks in Kokshal Segment, Southwestern Tianshan Mountains. *Geol. Rev.* **2007**, *53*, 743–754. [\[CrossRef\]](#)
19. Long, L.; Gao, J.; Xiong, X.; Qian, Q. The Geochemical Characteristics and the Age of the Kulelake Ophiolite in the Southern Tianshan. *Acta Petrol. Sin.* **2006**, *22*, 65–73. [\[CrossRef\]](#)
20. Xu, X.; Ma, Z.; Li, X.; He, S.; Yang, J. The Discovery of P-MORB in Jigen Area of Southwest Tianshan Mountains and Its Tectonic Implications. *Acta Petrol. Et Mineral.* **2003**, *22*, 245–253. [\[CrossRef\]](#)
21. Zhao, T.; Zhu, Z. Spatiotemporal Distribution of Ophiolite in Xinjiang and Constraints on Accretionary Orogenic Processes. *Xinjiang Geol.* **2021**, *39*, 21–29. [\[CrossRef\]](#)
22. Zhang, L.; Ai, Y.; Li, Q.; Li, X.; Song, S.; Wei, C. The Formation and Tectonic Evolution of UHP Metamorphic Belt in Southwestern Tianshan, Xinjiang. *Acta Petrol. Sin.* **2005**, *21*, 1029–1038. [\[CrossRef\]](#)
23. Li, Y.; Sun, L.; Wu, H.; Wang, G.; Yang, C.; Peng, G. Permo-Carboniferous Radiolaria from the Wupatarkan Group, West Terminal of Chinese South Tianshan. *Chin. J. Geol.* **2005**, *40*, 220–226. [\[CrossRef\]](#)
24. Li, Y.; Wang, Z.; Mai, G.; Wu, H.; Huang, Z.; Tan, Z. New Discovery of Radiolarian Fossils from Aiktik Group at in Tarim Basin and Its Significance. *Xinjiang Pet. Geol.* **2002**, *23*, 496–500. [\[CrossRef\]](#)

25. Huang, H.; Zhang, Z.; Kusky, T.; Zhang, D.; Hou, T.; Liu, J.; Zhao, Z. Geochronology and Geochemistry of the Chuanwulu Complex in the South Tianshan, Western Xinjiang, NW China: Implications for Petrogenesis and Phanerozoic Continental Growth. *Lithos* **2012**, *140–141*, 66–85. [[CrossRef](#)]
26. Wang, C.; Liu, L.; Luo, J.; Che, Z.; Teng, Z.; Cao, X.; Zhang, J. Late Paleozoic Post-Coilisional Magmatism in the Southwestern Tianshan Orogenic Belt, Take the Baleigong Pluton in the Kokshal Region as an Example. *Acta Geol. Sin.* **2007**, *23*, 1830–1840. [[CrossRef](#)]
27. Huang, H.; Wang, T.; Qin, Q.; Tong, Y.; Guo, L.; Zhang, L.; Huo, J.; Song, P. Geochronology and Zircon Hf Isotope of Baleigong Granitic Pluton in the Western Part of the South Tianshan Mountains: Petrogenesis and Implications for Tectonic Evolution. *Acta Petrol. Mineral.* **2015**, *34*, 971–990. [[CrossRef](#)]
28. Yang, F.; Wang, L.; Ye, J.; Fu, X.; Li, H. Zircon U-Pb Ages of Granites in the Houshibulak Area, Xinjiang. *Reg. Geol. China.* **2001**, *20*, 267–274. [[CrossRef](#)]
29. Zhang, C.; Xu, Y.; Li, Z.; Wang, H.; Ye, H. Diverse Permian Magmatism in the Tarim Block NW China: Genetically Linked to the Permian Tarim Mantle Plume? *Lithos* **2010**, *119*, 537–552. [[CrossRef](#)]
30. Gao, J.; Long, L.; Qian, Q.; Huang, D.; Su, W.; Reiner, K. South Tianshan: A Late Paleozoic or a Triassic Orogen? *Acta Petrol. Sin.* **2006**, *22*, 1049–1061. [[CrossRef](#)]
31. Han, Y.; Zhao, G.; Sun, M.; Eizenhöfer, P.R.; Hou, W.; Zhang, X.; Liu, D.; Wang, B.; Zhang, G. Paleozoic Accretionary Orogenesis in the Paleo-Asian Ocean: Insights from Detrital Zircons from Silurian to Carboniferous Strata at the Northwestern Margin of the Tarim Craton. *Tectonics* **2015**, *34*, 334–351. [[CrossRef](#)]
32. Zhu, Z.; Li, J.; Dong, L.; Zhang, X.; Hu, J.; Wang, K. The Age Determination of Late Carboniferous Intrusions in Mangqisu Region and Its Constraints to the Closure of Oceanic Basin in South Tianshan, Xinjiang. *Acta Petrol. Sin.* **2008**, *24*, 2761–2766. (In Chinese with English abstract)
33. Li, J.; Wang, K.; Li, Y.; Sun, G.; Chu, C.; Li, L.; Zhu, Z. Geomorphological Features, Crustal Composition and Geological Evolution of the Tianshan Mountains. *Geol. Bull. China.* **2006**, *25*, 895–909. [[CrossRef](#)]
34. Han, B.; He, G.; Wang, X.; Guo, Z. Late Carboniferous Collision between the Tarim and Kazakhstan–Yili Terranes in the Western Segment of the South Tian Shan Orogen, Central Asia, and Implications for the Northern Xinjiang, Western China. *Earth-Sci. Rev.* **2011**, *109*, 74–93. [[CrossRef](#)]
35. Gao, J.; Long, L.; Klemd, R.; Qian, Q.; Liu, D.; Xiong, X.; Su, W.; Liu, W.; Wang, Y.; Yang, F. Tectonic Evolution of the South Tianshan Orogen and Adjacent Regions, NW China: Geochemical and Age Constraints of Granitoid Rocks. *Int. J. Earth Sci.* **2009**, *98*, 1221–1238. [[CrossRef](#)]
36. Li, Y.; Yang, H.; Zhao, Y.; Luo, J.; Zheng, D.; Liu, Y. Tectonic Framework and Evolution of South Tianshan, NW China. *Geotechnica Metall.* **2009**, *31*, 94–104. [[CrossRef](#)]
37. Brookfield, M.E. Geological Development and Phanerozoic Crustal Accretion in the Western Segment of the Southern Tien Shan (Kyrgyzstan, Uzbekistan and Tajikistan). *Tectonophysics* **2000**, *328*, 1–14. [[CrossRef](#)]
38. Ma, L.; Zhang, Z.; Dong, S.; Zhang, S.; Zhang, D.; Huang, H.; Xue, C. Yingmailai Granitic Intrusion in the Southern Tianshan: Magnetite-Series or Ilmenite-Series? *Geoscience* **2009**, *23*, 1039–1048. [[CrossRef](#)]
39. Zhang, L.; Ai, Y.; Li, X.; Rubatto, D.; Song, B.; Williams, S.; Song, S.; Ellis, D.; Liou, J.G. Triassic Collision of Western Tianshan Orogenic Belt, China: Evidence from SHRIMP U–Pb Dating of Zircon from HP/UHP Eclogitic Rocks. *Lithos* **2007**, *96*, 266–280. [[CrossRef](#)]
40. Xiao, W.; Windley, B.F.; Sun, S.; Li, J.; Huang, B.; Han, C.; Yuan, C.; Sun, M.; Chen, H. A Tale of Amalgamation of Three Permo-Triassic Collage Systems in Central Asia: Oroclines, Sutures, and Terminal Accretion. *Annu. Rev. Earth Planet. Sci.* **2015**, *43*, 477–507. [[CrossRef](#)]
41. Xiao, W.; Huang, B.; Han, C.; Sun, S.; Li, J. A Review of the Western Part of the Altai: A Key to Understanding the Architecture of Accretionary Orogens. *Gondwana Res.* **2010**, *18*, 253–273. [[CrossRef](#)]
42. Zhang, C.; Zou, H. Permian A-Type Granites in Tarim and Western Part of Central Asian Orogenic Belt (CAOB): Genetically Related to a Common Permian Mantle Plume? *Lithos* **2013**, *172–173*, 47–60. [[CrossRef](#)]
43. Sun, L.; Wang, Y.; Fan, W.; Zi, J. A Further Discussion of the Petrogenesis and Tectonic Implication of the Mazhashan Syenites in the Bachu Area. *J. Jilin Univ.* **2008**, *38*, 8–20. [[CrossRef](#)]
44. Wei, X.; Xu, Y. Petrogenesis of Xiaohaizi Syenite Complex from Bachu Area, Tarim. *Acta Petrol. Sin.* **2011**, *27*, 2984–3004. (In Chinese with English abstract)
45. Huang, H.; Zhang, Z.; Zhang, D.; Du, H.; Ma, L.; Kang, J.; Xue, C. Petrogenesis of Late Carboniferous to Early Permian Granitoid Plutons in the Chinese South Tianshan: Implications for Crustal Accretion. *Acta Geol. Sin.* **2011**, *85*, 1305–1333. (In Chinese with English abstract) [[CrossRef](#)]
46. Huang, H.; Zhang, Z.; Santosh, M.; Zhang, D. Geochronology, Geochemistry and Metallogenic Implications of the Boziguo'er Rare Metal-Bearing Peralkaline Granitic Intrusion in South Tianshan, NW China. *Ore Geol. Rev.* **2014**, *61*, 157–174. [[CrossRef](#)]
47. Wang, C.; Luo, J.; Che, Z.; Liu, L.; Zhang, J. Geochemical Characteristics and U-Pb LA-ICP-MS Zircon Dating of the Oxidaban Pluton from Xinjiang, China: Implications for a Paleozoic Oceanic Subduction Process in Southwestern Tianshan. *Acta Geol. Sin.* **2009**, *83*, 272–283.
48. Konopelko, D.; Biske, G.; Seltmann, R.; Eklund, O.; Belyatsky, B. Hercynian Post-Collisional A-Type Granites of the Kokshaal Range, Southern Tien Shan, Kyrgyzstan. *Lithos* **2007**, *97*, 140–160. [[CrossRef](#)]

49. Solomovich, L.I. Postcollisional Magmatism in the South Tien Shan Variscan Orogenic Belt, Kyrgyzstan: Evidence for High-Temperature and High-Pressure Collision. *J. Asian Earth Sci.* **2007**, *30*, 142–153. [[CrossRef](#)]
50. Solomovich, L.I.; Trifonov, B.A. Postcollisional Granites in the South Tien Shan Variscan Collisional Belt, Kyrgyzstan. *J. Asian Earth Sci.* **2002**, *21*, 7–21. [[CrossRef](#)]
51. Konopelko, D.; Seltmann, R.; Biske, G.; Lepekhina, E.; Sergeev, S. Possible Source Dichotomy of Contemporaneous Post-Collisional Barren I-Type versus Tin-Bearing A-Type Granites, Lying on Opposite Sides of the South Tien Shan Suture. *Ore Geol. Rev.* **2009**, *35*, 206–216. [[CrossRef](#)]
52. Sengör, A.M.C.; Natal'in, B.A. Turcic-Type Orogeny and Its Role in the Making of the Continental Crust. *Annu. Rev. Earth Planet. Sci.* **1996**, *24*, 263–337. [[CrossRef](#)]
53. Kröner, A.; Alexeiev, D.V.; Rojas-Agramonte, Y.; Hegner, E.; Wong, J.; Xia, X.; Belousova, E.; Mikolaichuk, A.V.; Seltmann, R.; Liu, D.; et al. Mesoproterozoic (Grenville-Age) Terranes in the Kyrgyz North Tianshan: Zircon Ages and Nd–Hf Isotopic Constraints on the Origin and Evolution of Basement Blocks in the Southern Central Asian Orogen. *Gondwana Res.* **2013**, *23*, 272–295. [[CrossRef](#)]
54. Dong, Y.; Zhang, G.; Neubauer, F.; Liu, X.; Hauzenberger, C.; Zhou, D.; Li, W. Syn- and Post-Collisional Granitoids in the Central Tianshan Orogen: Geochemistry, Geochronology and Implications for Tectonic Evolution. *Gondwana Res.* **2011**, *20*, 568–581. [[CrossRef](#)]
55. Bureau of Geology and Mineral Resources of Xinjiang Uygur Autonomous Region. *Regional Geology of Xinjiang Uygur Autonomous Region*; Geological Publishing House: Beijing, China, 1993; ISBN 7-116-01225-5.
56. Xu, Y.; Yin, J.; Xiao, K.; Xu, H.; Fang, J.; Fan, M. Skarn Mineral Characteristics of the Ahetala Copper Deposit and Its Geological Significance. *Rock Miner. Anal.* **2022**, *41*, 575–585. [[CrossRef](#)]
57. Xu, Y.; Yin, J.; An, B.; Li, S.; Zhao, C.; Xu, H.; Fang, J. Study on the Characteristics of Garnets in Ahetala Copper Deposit. *J. Chin. Electron Microsc. Soc.* **2018**, *37*, 339–347. [[CrossRef](#)]
58. Liu, Y.; Hu, Z.; Zong, K.; Gao, C.; Gao, S.; Xu, J.; Chen, H. Reappraisal and Refinement of Zircon U-Pb Isotope and Trace Element Analyses by LA-ICP-MS. *Chin. Sci. Bull.* **2010**, *55*, 1535–1546. [[CrossRef](#)]
59. Smith, J.V. *Feldspar Mineral*; Springer: Berlin/Heidelberg, Germany, 1974.
60. Foster, M.D. *Interpretation of the Composition of Trioctahedral Micas*; United States Government Printing Office: Washington, DC, USA, 1960; pp. 11–49.
61. Leake, B.E.; Woolley, A.R.; Arps, C.E.S.; Birch, W.D.; Gilbert, M.C.; Grice, J.D.; Hawthorne, F.C.; Kato, A.; Kisch, H.J.; Krivovichev, V.G.; et al. Nomenclature Of Amphiboles: Report Of The Subcommittee On Amphiboles Of The International Mineralogical Association, Commission On New Minerals And Mineral Names. *Mineral. Mag.* **1997**, *61*, 295–310. [[CrossRef](#)]
62. Wilson, M. *Igneous Petrogenesis A Global Tectonic Approach*; Springer: Berlin/Heidelberg, Germany, 1989; ISBN 978-0-412-53310-5.
63. Maniar, P.D.; Piccoli, P.M. Tectonic Discrimination of Granitoids. *Geol. Soc. Am. Bull.* **1989**, *101*, 635–643. [[CrossRef](#)]
64. Peccerillo, A.; Taylor, S.R. Geochemistry of Eocene Calc-Alkaline Volcanic Rocks from the Kastamonu Area, Northern Turkey. *Contr. Mineral. Petrol.* **1976**, *58*, 63–81. [[CrossRef](#)]
65. Sun, S.-S.; McDonough, W.F. Chemical and Isotopic Systematics of Oceanic Basalts: Implications for Mantle Composition and Processes. *Geol. Soc. Lond. Spec. Publ.* **1989**, *42*, 313–345. [[CrossRef](#)]
66. Bonin, B. A-Type Granites and Related Rocks: Evolution of a Concept, Problems and Prospects. *Lithos* **2007**, *97*, 1–29. [[CrossRef](#)]
67. Collins, W.J.; Beams, S.D.; White, A.J.R.; Chappell, B.W. Nature and Origin of A-Type Granites with Particular Reference to Southeastern Australia. *Contr. Mineral. Petrol.* **1982**, *80*, 189–200. [[CrossRef](#)]
68. Whalen, J.B.; Currie, K.L.; Chappell, B.W. A-Type Granites: Geochemical Characteristics, Discrimination and Petrogenesis. *Contrib. Miner. Pet.* **1987**, *95*, 407–419. [[CrossRef](#)]
69. King, P.L.; White, A.J.R.; Chappell, B.W.; Allen, C.M. Characterization and Origin of Aluminous A-Type Granites from the Lachlan Fold Belt, Southeastern Australia. *J. Petrol.* **1997**, *38*, 21. [[CrossRef](#)]
70. Chappell, B.W.; White, A.J.R. Two Contrasting Granite Types: 25 Years Later. *Aust. J. Earth Sci.* **2001**, *48*, 489–499. [[CrossRef](#)]
71. Yang, Z.; Lu, Y.; Hou, Z.; Chang, Z. High-Mg Diorite from Qulong in Southern Tibet: Implications for the Genesis of Adakite-like Intrusions and Associated Porphyry Cu Deposits in Collisional Orogens. *J. Petrol.* **2015**, *56*, 227–254. [[CrossRef](#)]
72. Chappell, B.W. Aluminium Saturation in I- and S-Type Granites and the Characterization of Fractionated Haplogranites. *Lithos* **1999**, *46*, 535–551. [[CrossRef](#)]
73. Chappell, B.W.; White, A.J.R. I- and S-Type Granites in the Lachlan Fold Belt. *Trans. R. Soc. Edinb. Earth Sci.* **1992**, *83*, 1–26. [[CrossRef](#)]
74. Zhang, R.; He, W.; Gao, X.; Li, M. Magma Mixing of the Daocheng Batholith of Western Sichuan: Mineralogical Evidences. *Earth Sci. Front.* **2018**, *25*, 226–239. [[CrossRef](#)]
75. Ding, X. Study of Typomorphic Characteristics of Micas From Granitoids in Central-Southern Xizang and Their Geological Significance. *Bull. Inst. Miner. Depos. Chin. Acad. Geol. Sci.* **1988**, *1*, 33–49.
76. Fu, J. Chemical Composition of Biotite in Porphyry Copper Deposit. *Geol. Explor.* **1981**, 18–21.
77. Xie, Y.; Zhang, Y. Peculiarities and Genetic Significance of Hornblende from Granite in the Hengduanshan Region. *Acta Mineral. Sin.* **1990**, *10*, 35–45. (In Chinese) [[CrossRef](#)]
78. Zhou, Z. The Origin of Intrusive Mass in Fengshandong, Hubei Province. *Acta Petrol. Sin.* **1986**, *2*, 59–70.

79. Green, T.H. Significance of Nb/Ta as an Indicator of Geochemical Processes in the Crust-Mantle System. *Chem. Geol.* **1995**, *120*, 347–359. [[CrossRef](#)]
80. Sami, M.; El Monsef, M.A.; Abart, R.; Toksoy-Köksal, F.; Abdelfadil, K.M. Unraveling the Genesis of Highly Fractionated Rare-Metal Granites in the Nubian Shield via the Rare-Earth Elements Tetrad Effect, Sr–Nd Isotope Systematics, and Mineral Chemistry. *ACS Earth Space Chem.* **2022**, *6*, 2368–2384. [[CrossRef](#)]
81. Li, L.; Zheng, Y.; Zhou, J. Dynamic Model for Pb Isotope Evolution in the Continental Crust of China. *Acta Petrol. Sin.* **2001**, *17*, 61–68.
82. Rapp, R.P.; Watson, E.B. Dehydration Melting of Metabasalt at 8–32 Kbar: Implications for Continental Growth and Crust-Mantle Recycling. *J. Petrol.* **1995**, *36*, 891–931. [[CrossRef](#)]
83. Fitton, J.G.; James, D.; Leeman, W.P. Basic Magmatism Associated with Late Cenozoic Extension in the Western United States: Compositional Variations in Space and Time. *J. Geophys. Res.* **1991**, *96*, 13693–13711. [[CrossRef](#)]
84. Laurent, O.; Martin, H.; Moyen, J.F.; Doucelance, R. The Diversity and Evolution of Late-Archean Granitoids: Evidence for the Onset of “Modern-Style” Plate Tectonics between 3.0 and 2.5 Ga. *Lithos* **2014**, *205*, 208–235. [[CrossRef](#)]
85. Jiang, C.; An, S. On Chemical Characteristics of Calcic Amphiboles From Igneous Rocks and Their Petrogenesis Significance. *J. Mineral. Petrol.* **1984**, *3*, 1–9. [[CrossRef](#)]
86. Allègre, C.J.; Minster, J.F. Quantitative Models of Trace Element Behavior in Magmatic Processes. *Earth Planet. Sci. Lett.* **1978**, *38*, 1–25. [[CrossRef](#)]
87. Schiano, P.; Monzier, M.; Eissen, J.-P.; Martin, H.; Koga, K.T. Simple Mixing as the Major Control of the Evolution of Volcanic Suites in the Ecuadorian Andes. *Contrib. Miner. Pet.* **2010**, *160*, 297–312. [[CrossRef](#)]
88. Liu, B.; Qian, Y. The Geologic Characteristics and Fluid Evolution in the Three High-Pressure Metamorphic Belts of Eastern Tianshan. *Acta Petrol. Sin.* **2003**, *19*, 283–296. [[CrossRef](#)]
89. Gao, J.; Klemd, R. Formation of HP–LT Rocks and Their Tectonic Implications in the Western Tianshan Orogen, NW China: Geochemical and Age Constraints. *Lithos* **2003**, *66*, 1–22. [[CrossRef](#)]
90. Li, Q.; Zhang, L. The P–T Path and Geological Significance of Low-Pressure Granulite-Facies Metamorphism in Muzhaerte, Southwest Tianshan. *Acta Petrol. Sin.* **2004**, *20*, 583–594.
91. Liu, B.; Chen, Z.; Ren, R.; Han, B.; Su, L. Timing of the South Tianshan Suture Zone: New Evidence of Zircon Ages from the Granitic Plutons in Kokshal Area. *Geol. Bull. China.* **2013**, *32*, 1371–1384.
92. Abdel-Rahman, A.-F.M. Nature of Biotites from Alkaline, Calc-Alkaline, and Peraluminous Magmas. *J. Petrol.* **1994**, *35*, 525–541. [[CrossRef](#)]
93. Abdelfadil, K.M.; Saleh, G.M.; Putiš, M.; Sami, M. Mantle Source Characteristics of the Late Neoproterozoic Post-Collisional Gabbroic Intrusion of Wadi Abu Hadieda, North Arabian-Nubian Shield, Egypt. *J. Afr. Earth Sci.* **2022**, *194*, 104607. [[CrossRef](#)]
94. Sylvester, P.J. Post-Collisional Strongly Peraluminous Granites. *Lithos* **1998**, *45*, 29–44. [[CrossRef](#)]
95. Hou, Z.; Gao, Y.; Meng, X.; Qu, X.; Huang, W. Genesis of Adakitic Porphyry and Tectonic Controls on the Gangdese Miocene Porphyry Copper Belt in the Tibetan Orogen. *Acta Petrol. Sin.* **2004**, *20*, 239–248. [[CrossRef](#)]
96. Pearce, J.A.; Harris, N.B.W.; Tindle, A.G. Trace Element Discrimination Diagrams for the Tectonic Interpretation of Granitic Rocks. *J. Petrol.* **1984**, *25*, 956–983. [[CrossRef](#)]
97. Batchelor, R.A.; Bowden, P. Petrogenetic Interpretation of Granitoid Rock Series Using Multicationic Parameters. *Chem. Geol.* **1985**, *48*, 43–55. [[CrossRef](#)]
98. Harris, N.B.W.; Pearce, J.A.; Tindle, A.G. Geochemical Characteristics of Collision-Zone Magmatism. *SP* **1986**, *19*, 67–81. [[CrossRef](#)]
99. Chen, C.; Lu, H.; Jia, D.; Cai, D.; Wu, S. Closing History of the Southern Tianshan Oceanic Basin, Western China: An Oblique Collisional Orogeny. *Tectonophysics* **1999**, *302*, 23–40. [[CrossRef](#)]
100. Kong, W.; Zhang, Z.; Huang, H.; Cheng, Z.; Santosh, M. Geochemistry and Zircon U–Pb Geochronology of the Oxidaban Intrusive Complex: Implication for Paleozoic Tectonic Evolution of the South Tianshan Orogenic Belt, China. *Lithos* **2019**, *324–325*, 265–279. [[CrossRef](#)]
101. Huang, H.; Zhang, Z.; Santosh, M.; Zhang, D.; Wang, T. Petrogenesis of the Early Permian Volcanic Rocks in the Chinese South Tianshan: Implications for Crustal Growth in the Central Asian Orogenic Belt. *Lithos* **2015**, *228–229*, 23–42. [[CrossRef](#)]
102. Zhang, X.; Zhao, G.; Eizenhöfer, P.R.; Sun, M.; Han, Y.; Hou, W.; Liu, D.; Wang, B.; Liu, Q.; Xu, B. Paleozoic Magmatism and Metamorphism in the Central Tianshan Block Revealed by U–Pb and Lu–Hf Isotope Studies of Detrital Zircons from the South Tianshan Belt, NW China. *Lithos* **2015**, *233*, 193–208. [[CrossRef](#)]
103. Han, Y.; Zhao, G.; Sun, M.; Eizenhöfer, P.R.; Hou, W.; Zhang, X.; Liu, Q.; Wang, B.; Liu, D.; Xu, B. Late Paleozoic Subduction and Collision Processes during the Amalgamation of the Central Asian Orogenic Belt along the South Tianshan Suture Zone. *Lithos* **2016**, *246–247*, 1–12. [[CrossRef](#)]
104. Yu, X.; Qin, Q.; Huang, H.; Wang, T.; Zhang, Z.; Tong, Y.; Guo, L.; Song, P. Genesis and Tectonic Significance of the Mangqisu Pluton in the South Tianshan: Evidence from Geochronology, Geochemistry, and Nd–Hf Isotopes. *Acta Geol. Sin.* **2020**, *94*, 2893–2918.